Electronic Supplementary Information to: Effective transport properties in porous composites applied to MIEC SOC electrodes

Philip Marmet,[*a,b] Lorenz Holzer,[a] Thomas Hocker,[a] Gernot K. Boiger,[a] and Joseph M. Brader[b]

[a] *Zurich University of Applied Sciences, Institute of Computational Physics, CH-8400 Winterthur, Switzerland. E-mail: mame@zhaw.ch*
[b] *Department of Physics, University of Fribourg, CH-1700 Fribourg, Switzerland.*

Contents

A Illustration of the influence of porosity, composition, wetting behaviour and interface resistance on the composite conductivity **2**

B Details for the illustration of composite conductivity effects **5**
B.1 Construction parameters for the virtual PGM microstructures with different wetting behaviour 5
B.2 Effect of an interface resistance between the two solid phases 5

C Derivations for the semi-analytical models to predict the composite conductivity **7**
C.1 Derivations for the Maxwell model 7
C.2 Derivations for the Xu model 7
C.3 Derivation and validation of the relative interface resistivity used in the MST model 8

D Model validation for the prediction of the composite conductivity **10**
D.1 Predictions with the Maxwell model 11
D.1.1 Validation for conductivity ratio $\lambda = 0.1$ 11
D.1.2 Validation for conductivity ratio $\lambda = [0.5, 0.01, 0.0001]$ 11
D.2 Predictions with the Xu model 15
D.2.1 Validation for conductivity ratio $\lambda = 0.1$ 15
D.2.2 Validation for conductivity ratio $\lambda = [0.5, 0.01, 0.0001]$ 16
D.3 Predictions with the MST model 19
D.3.1 Validation for conductivity ratio $\lambda = 0.1$ 19
D.3.2 Validation for conductivity ratio $\lambda = [0.5, 0.01, 0.0001]$ 20
D.4 Validation of the composite conductivity predictions with further reference data 23
D.4.1 Validation of the predictions for a dataset of pure PGM-structures 23
D.4.2 Validation of the predictions for a dataset of virtual sphere-packing structures 26

References **29**

A Illustration of the influence of porosity, composition, wetting behaviour and interface resistance on the composite conductivity

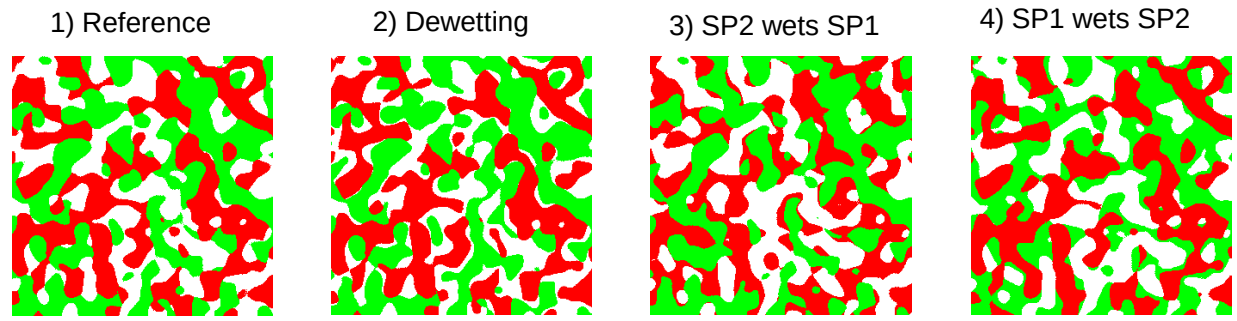

(a) Porosity $\varepsilon = 30\,\%$, $\phi_{SP1} : \phi_{SP2} = 50 : 50$

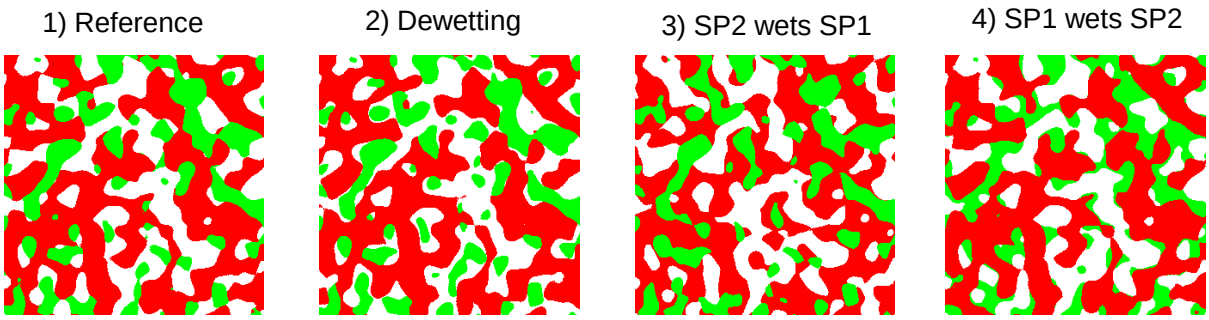

(b) Porosity $\varepsilon = 30\,\%$, $\phi_{SP1} : \phi_{SP2} = 30 : 70$

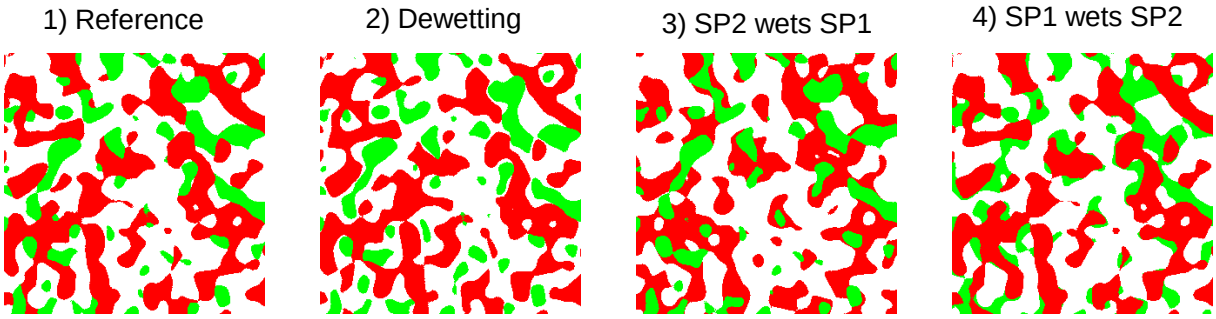

(c) Porosity $\varepsilon = 50\,\%$, $\phi_{SP1} : \phi_{SP2} = 30 : 70$

Fig. 1 Orthoslices of 3D microstructures with different wetting behaviours (1-4), porosities and compositions (a-c). Colour code: SP1=green, SP2 = red, pore = white. The corresponding parameters for the construction of the presented PGM structures according to Marmet et al.[1] are summarized in the ESI section A.1.

In this section, basic effects related to the composite conductivity are studied based on numerical simulations on general PGM structures. The virtual PGM structures are generated using the PGM-app reported in a previous publication (Marmet et al.[1]). Thereby, the PGM parameters are chosen in order to obtain microstructures with different porosities, compositions and wetting behaviours. The corresponding PGM construction parameters are summarized in section A.1 of the ESI. The composite conductivities are then determined for these structures by numerical simulations using GeoDict as described in a previous publication (Marmet et al.[2]).

Additionally, also the influence of a potential interface resistance between the two solid phases SP1 and SP2 is studied.

In Fig. 1, 2D orthoslices of 3D PGM structures with different porosities, compositions and wetting behaviours are reported. For a better recognition of the microstructure features, only one quarter of the or-

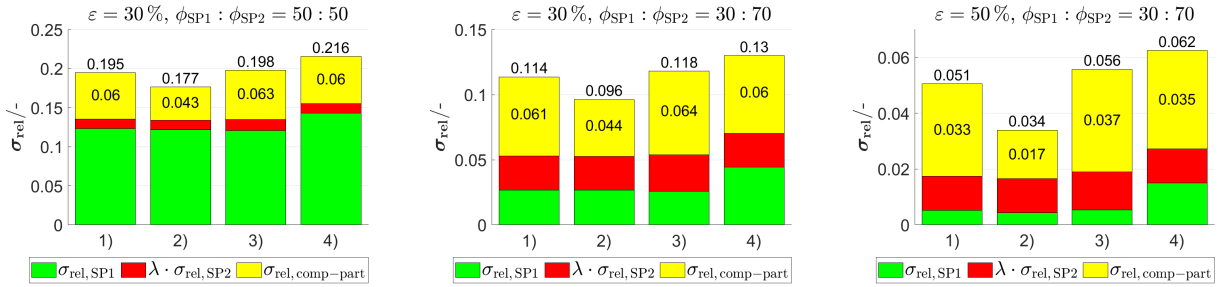

(a) Porosity $\varepsilon = 30\,\%$, $\phi_{SP1} : \phi_{SP2} = 50 : 50$

(b) Porosity $\varepsilon = 30\,\%$, $\phi_{SP1} : \phi_{SP2} = 30 : 70$

(c) Porosity $\varepsilon = 50\,\%$, $\phi_{SP1} : \phi_{SP2} = 30 : 70$

Fig. 2 Relative composite conductivity for $\lambda = 0.1$ and the corresponding contributions, the single-phase conductivities $\sigma_{rel,SP1}$ and $\lambda \cdot \sigma_{rel,SP2}$, and the composite conductivity effect $\sigma_{rel,comp-part}$, for PGM microstructures with different wetting behaviours (1-4), porosities and compositions (a-c). The numbers on the top are the relative composite conductivities and the numbers within the yellow parts the composite conductivity effect.

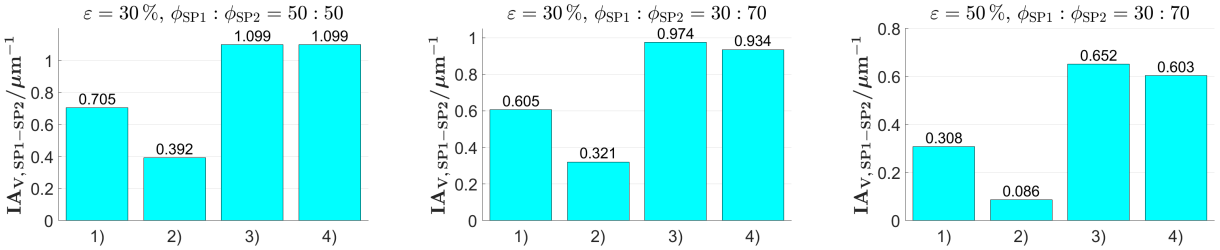

(a) Porosity $\varepsilon = 30\,\%$, $\phi_{SP1} : \phi_{SP2} = 50 : 50$

(b) Porosity $\varepsilon = 30\,\%$, $\phi_{SP1} : \phi_{SP2} = 30 : 70$

(c) Porosity $\varepsilon = 50\,\%$, $\phi_{SP1} : \phi_{SP2} = 30 : 70$

Fig. 3 Volume specific interface area SP1-SP2 for the PGM microstructures with different wetting behaviours (1-4), porosities and compositions (a-c).

thoslices is shown and larger structures of 600^3 voxels are used for the characterization. The following cases for the wetting behaviour are studied:

1) Neutral wetting behaviour for the solid phases (reference).
2) Dewetting of the two solid phases (i.e., the two solid phases do not like to touch each other).
3) SP2 wets SP1 (i.e., SP2 partially encloses SP1 and is more present at the surface).
4) SP1 wets SP2 (i.e., SP1 partially encloses SP2 and is more present at the surface).

For these microstructures, the relative composite conductivities are reported in Fig. 2. Thereby, the three contributions to the composite conductivity presented in section 2.3.3 in the main article (single-phase conductivity of SP1, single-phase conductivity of SP2 and a composite conductivity part) are distinguished. Note that the composite conductivity part is calculated as the difference of the relative composite conductivity and the single-phase conductivity (and not predicted with the MST model) by rearranging Eq. 16 of the main article to $\sigma_{rel,comp-part,Rint} = \sigma_{rel,comp} - \sigma_{rel,SP1} - \lambda \cdot \sigma_{rel,SP2}$. In Fig. 3, the corresponding volume specific interface area SP1-SP2 is reported to check for potential correlations.

For the reference microstructure with neutral wetting behaviour with porosity $\varepsilon = 30\,\%$ and $\phi_{SP1} : \phi_{SP2} = 50 : 50$ (Fig. 1 (a-1)), the main contribution to the relative composite conductivity is the single-phase conductivity of SP1, while the contribution of the single-phase conductivity of SP2 with the same phase volume fraction is ten times smaller, corresponding to conductivity ratio $\lambda = 0.1$ (Fig. 2 (a-1)). The contribution of the composite conductivity effect is about 31 %. For the reference microstructure with porosity $\varepsilon = 30\,\%$ and $\phi_{SP1} : \phi_{SP2} = 30 : 70$ (Fig. 1 (b-1)), the single-phase conductivities of SP1 and SP2 have similar contributions, because the lower intrinsic conductivity of SP2 is compensated by its larger phase volume fraction (Fig. 2 (b-1)). The composite conductivity effect contributes about 54 % to the relative composite conductivity and

thus is considerably more important compared to the case (a-1). However, the relative composite conductivity is reduced by 42 % compared to the case (a-1). The same but even more pronounced tendencies can be observed for the reference microstructure with porosity $\varepsilon = 50\,\%$ and $\phi_{\mathrm{SP1}} : \phi_{\mathrm{SP2}} = 30 : 70$ (Fig. 1 (c-1)). The contribution of the single-phase conductivity of SP1 is very small because it approaches the percolation threshold (Fig. 2 (c-1)). The composite conductivity effect contributes about 65 % to the relative composite conductivity. However, the relative composite conductivity is reduced to about one quarter compared to the case (a-1).

The effects from the different wetting behaviours are qualitatively identical for the different porosities and compositions, but again more pronounced for higher porosity and lower SP1-content. For the dewetting case 2) the contributions of the single-phase conductivities are almost unchanged compared to the reference case 1) with neutral wetting for all porosities and composition. In contrast, the composite conductivity effect is considerably reduced, which correlates well with the reduced volume specific interface area SP1-SP2 reported in Fig. 3. The influence is most pronounced for $\varepsilon = 50\,\%$, $\phi_{\mathrm{SP1}} : \phi_{\mathrm{SP2}} = 30 : 70$ (Fig. 2 (c-2)), where the composite conductivity effect is halved compared to the reference case. For the wetting cases 3) and 4), the single-phase conductivity of the phase wetting the other is increased, resulting also in an increase of the corresponding relative composite conductivities. This increase is due to the better connection of the wetting phase, which can be observed as well by visual comparison of e.g., Fig. 1 (c-1) and (c-4). The effect on the relative composite conductivity is more pronounced for the case SP1 wets SP2, because SP1 owns the higher conductivity (e.g., Fig. 2 (a-4)). Thereby, the composite conductivity effect is only marginally increased, despite the considerable increase of the volume specific interface area SP1-SP2 compared to the reference case. For example, the composite conductivity effect for case 4) compared to case 1) in Fig. 2 c) increases only about 6 %, despite the fact that the volume specific interface area SP1-SP2 is doubled (Fig. 3 c)). Thus, the interface area is not the limiting factor in this case.

In the current study it is assumed that there is no interface resistance between the two solid phases. However, there is yet no literature data available, which would proof this assumption for titanate-CGO composites. Hence, a study for the effect of an interface resistance between SP1 and SP2 on the relative composite conductivity is reported in section A.2 of the ESI. The findings of this study can be summarized as follows:

- An interface resistance between SP1 and SP2 only affects the composite conductivity effect $\sigma_{\mathrm{rel,comp-part}}$, but not the contributions from the single-phase conductivities. Thus, for a very large area specific interface resistance ρ_{int} the composite conductivity effect vanishes and the remaining conductivity is simply the sum of the single-phase conductivities of the two solid phases according to Eq. 16 in the main article.

- According to Eq. 20 of the main article, the relative interface resistivity scales with ν_i, which relates the area specific interface resistance ρ_{int} to the intrinsic conductivity. Thus, a large area specific interface resistance especially reduces the relative composite conductivity in combination with a high intrinsic conductivity.

- The relative interface resistivity is inverse proportional to the characteristic size of the microstructure features, as derived in section A.2 of the ESI. Thus, for fine porous structures the interface resistance has a larger impact on the composite conductivity compared to coarser structures because of the higher density of interfaces.

For a quantitative description of interface resistance effects, appropriate material properties for specific material combinations would be needed, which are currently not available in the literature. Nevertheless, the current study provides a theoretical basis for the systematic study of such effects.

B Details for the illustration of composite conductivity effects

B.1 Construction parameters for the virtual PGM microstructures with different wetting behaviour

The construction parameters for the PGM structures presented in appendix A are reported in table 1. The porosities and compositions are additionally varied and directly reported in appendix A.

Table 1 Construction parameters for the PGM structures presented in appendix A. The threshold angles α, β and γ control the wetting behaviour. SD_{GRF1} and SD_{GRF2} are the standard deviations (characteristic length) of the two Gaussian random fields. The PGM approach is presented in a previous publication (Marmet et al.[1]).

Description	Case-number	α	β	γ	Voxel size	SD_{GRF1}	SD_{GRF2}
Reference (neutral wetting)	1	45°	0°	0°	40 nm	10 vox	10 vox
Dewetting	2	45°	20°	-20°	40 nm	10 vox	10 vox
SP2 wets SP1	3	80°	-40°	0°	40 nm	10 vox	10 vox
SP1 wets SP2	4	10°	0°	40°	40 nm	10 vox	10 vox

B.2 Effect of an interface resistance between the two solid phases

The effect of an interface resistance between SP1 and SP2 on the relative composite conductivity part for the different wetting behaviours is reported in Fig. 4 a). The corresponding relative ionic composite conductivities are reported in Fig. 6 in section C.3, where the data is used for validation of the MST model including an interface resistance between the two solid phases. For a $\nu_{\mathrm{ion}} \to 0$, the interface resistance is negligible and for $\nu_{\mathrm{ion}} \to \infty$ the composite conductivity effect vanishes and the remaining conductivity is simply the sum of the single-phase conductivities of the two solid phases according to Eq. 17 of the main article. For the different wetting behaviours, the composite conductivity part starts at different values for $\nu_{\mathrm{ion}} \to 0$, but their course as a function of ν_{ion} is very similar, and they tend to the same asymptotic value for $\nu_{\mathrm{ion}} \to \infty$. In Fig. 4 b), the effect of a structural scaling is reported. For a scaling factor of 0.1 the same relative composite conductivity part is observed as for a scaling factor of 1 with a ten times lower interface resistance and vice versa for a scaling factor of 10. This can be understood by considering the analytical estimation of the interface resistivity in Eq. 20 of the main article. The interface resistivity is indirect proportional to the volume specific SP1-SP2 interface area and to the square of the characteristic bulge-size r_{max} of the structure, as stated in Eq. 1. As the volume specific interface area itself scales indirect proportional to r_{max} (i.e., $IA_{\mathrm{V,SP1-SP2}} \propto 1/r_{\mathrm{max}}$), the interface resistivity finally scales indirect proportional to r_{max}.

$$\rho_{\mathrm{rel,I,SP1-SP2},i} \propto \frac{\nu_i}{IA_{\mathrm{V,SP1-SP2}} \cdot (r_{\mathrm{max}})^2} \propto \frac{\nu_i}{r_{\mathrm{max}}} \tag{1}$$

For example, if the structure is scaled by a factor of 0.1, there are a factor of 100 more serial interface resistances but the interface area is only increased by a factor of 10, resulting in a total increase of the interface resistivity by a factor of 10 (see also illustration in Fig. 5). A mathematical derivation of this relation can be found in section C.3 of this ESI. Additionally, Eq. 1 shows that the relative resistivity scales proportional to ν_i which relates the area specific interface resistance to the intrinsic conductivity. Thus, a scaling of ν_i by a factor of 10 corresponds to a scaling of the structure by a factor of 0.1.

In summary, the effect of the interface resistance between SP1 and SP2 is especially relevant for very small characteristic structure sizes (nano-powders) and for a large area specific interface resistance between SP1 ans SP2 in combination with a high intrinsic conductivity of the solid phases (i.e., large values of ν_i). For a quantitative description, appropriate material properties for specific material combinations would be needed, which are currently not available in the literature. Nevertheless, the current study provides a theoretical basis for the systematic study of such effects.

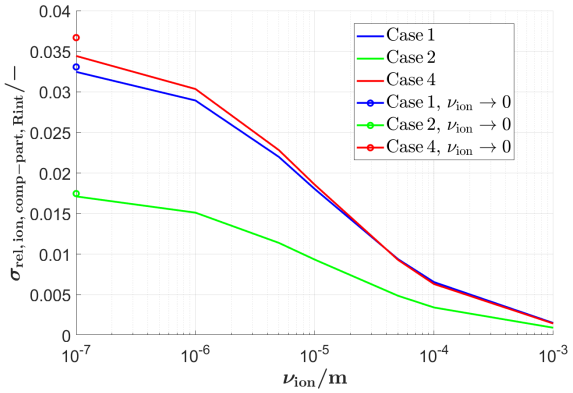

(a) Variation of the wetting.

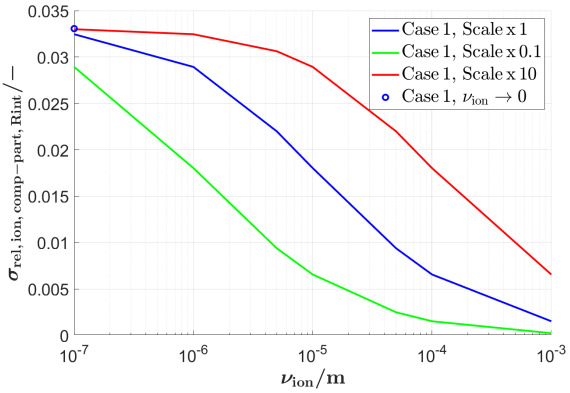

(b) Scaling effects.

Fig. 4 Relative ionic composite conductivity part with interface resistance between SP1 and SP2 as a function of ν_{ion} (i.e., normalized area specific interface resistance) for a) different wetting behaviours (case 1, case 2 and case 4) and b) for a scaling of the structure size for case 1. Note that a scaling of the structure size by a factor of 10 corresponds to a scaling of ν_{ion} by a factor of 0.1.

C Derivations for the semi-analytical models to predict the composite conductivity

C.1 Derivations for the Maxwell model

In order to formulate the relative ionic two-phase conductivity $\sigma_{\mathrm{rel,2ph,M2,ion}}$ with SP2 as the Matrix-phase, Eq. 11 of the main article has to be adapted as follows:

$$\frac{\sigma_{\mathrm{eff,2ph}}}{\sigma_{0,\mathrm{SP2}}} = \frac{2+\lambda_{\mathrm{ion}}^{-1}-2\left(1-\lambda_{\mathrm{ion}}^{-1}\right)\phi_{\mathrm{SP1,rel}}}{2+\lambda_{\mathrm{ion}}^{-1}+\left(1-\lambda_{\mathrm{ion}}^{-1}\right)\phi_{\mathrm{SP1,rel}}} \tag{2}$$

However, $\sigma_{\mathrm{rel,2ph,M2,ion}}$ shall be formulated in reference to the intrinsic ionic conductivity of SP1 $\sigma_{0,\mathrm{SP1}}$ (which is the superior intrinsic ionic conductivity), according to the definition in Eq. 4 of the main article:

$$\sigma_{\mathrm{rel,2ph,M2,ion}} = \frac{\sigma_{\mathrm{eff,2ph}}}{\sigma_{0,\mathrm{SP1}}} = \frac{\sigma_{\mathrm{eff,2ph}}}{\sigma_{0,\mathrm{SP2}}}\lambda_{\mathrm{ion}} \tag{3}$$

where the relation $\lambda_{\mathrm{ion}} = \frac{\sigma_{0,\mathrm{ion,SP2}}}{\sigma_{0,\mathrm{ion,SP1}}}$ (Eq. 5 of the main article) has been used. Therewith, the relative ionic two-phase conductivity $\sigma_{\mathrm{rel,2ph,M2,ion}}$ with SP2 as the Matrix-phase can be formulated as reported in Eq. 12 of the main article, which is repeated here for convenience:

$$\sigma_{\mathrm{rel,2ph,M2,ion}} = \frac{2+\lambda_{\mathrm{ion}}^{-1}-2\left(1-\lambda_{\mathrm{ion}}^{-1}\right)\phi_{\mathrm{SP1,rel}}}{2+\lambda_{\mathrm{ion}}^{-1}+\left(1-\lambda_{\mathrm{ion}}^{-1}\right)\phi_{\mathrm{SP1,rel}}}\lambda_{\mathrm{ion}} \tag{4}$$

C.2 Derivations for the Xu model

The Xu model[3] for the effective conductivity of a two-phase composite without porosity and with neglected intergranular resistance reported in Eq. 14 of the main article needs to be multiplied by M_{tot} to accounts for the porosity of the three-phase material system. Moreover it has to be divided by the intrinsic ionic conductivity of SP1 $\sigma_{0,\mathrm{ion,SP1}}$ in order to get the relative ionic composite conductivity:

$$\begin{aligned}\sigma^{\mathrm{Xu}}_{\mathrm{rel,ion,comp}} = &\frac{1}{4}\Bigg(3\,\phi_{\mathrm{SP2,rel}}\left(\sigma_{0,\mathrm{ion,SP2}}-\sigma_{0,\mathrm{ion,SP1}}\right)+\left(2\,\sigma_{0,\mathrm{ion,SP1}}-\sigma_{0,\mathrm{ion,SP2}}\right)\\ &+\sqrt{\left[3\,\phi_{\mathrm{SP2,rel}}\left(\sigma_{0,\mathrm{ion,SP2}}-\sigma_{0,\mathrm{ion,SP1}}\right)+\left(2\,\sigma_{0,\mathrm{ion,SP1}}-\sigma_{0,\mathrm{ion,SP2}}\right)\right]^2+8\,\sigma_{0,\mathrm{ion,SP2}}\sigma_{0,\mathrm{ion,SP1}}}\Bigg)\cdot\frac{M_{\mathrm{tot}}}{\sigma_{0,\mathrm{ion,SP1}}}\end{aligned} \tag{5}$$

Furthermore, the intrinsic ionic conductivity of SP2 $\sigma_{0,\mathrm{ion,SP2}}$ can be replaced using the relation $\lambda_{\mathrm{ion}} = \frac{\sigma_{0,\mathrm{ion,SP2}}}{\sigma_{0,\mathrm{ion,SP1}}}$:

$$\begin{aligned}\sigma^{\mathrm{Xu}}_{\mathrm{rel,ion,comp}} = &\frac{1}{4}\Bigg(3\,\phi_{\mathrm{SP2,rel}}\,\sigma_{0,\mathrm{ion,SP1}}\left(\lambda_{\mathrm{ion}}-1\right)+\sigma_{0,\mathrm{ion,SP1}}\left(2-\lambda_{\mathrm{ion}}\right)\\ &+\sqrt{\left[3\,\phi_{\mathrm{SP2,rel}}\,\sigma_{0,\mathrm{ion,SP1}}\left(\lambda_{\mathrm{ion}}-1\right)+\sigma_{0,\mathrm{ion,SP1}}\left(2-\lambda_{\mathrm{ion}}\right)\right]^2+8\,\lambda_{\mathrm{ion}}\,\sigma^2_{0,\mathrm{ion,SP1}}}\Bigg)\cdot\frac{M_{\mathrm{tot}}}{\sigma_{0,\mathrm{ion,SP1}}}\end{aligned} \tag{6}$$

By further transformation, $\sigma_{0,\mathrm{ion,SP1}}$ can be isolated:

$$\begin{aligned}\sigma^{\mathrm{Xu}}_{\mathrm{rel,ion,comp}} = &\frac{1}{4}\Bigg(3\,\phi_{\mathrm{SP2,rel}}\,\sigma_{0,\mathrm{ion,SP1}}\left(\lambda_{\mathrm{ion}}-1\right)+\sigma_{0,\mathrm{ion,SP1}}\left(2-\lambda_{\mathrm{ion}}\right)\\ &+\sigma_{0,\mathrm{ion,SP1}}\sqrt{\left[3\,\phi_{\mathrm{SP2,rel}}\left(\lambda_{\mathrm{ion}}-1\right)+\left(2-\lambda_{\mathrm{ion}}\right)\right]^2+8\,\lambda_{\mathrm{ion}}}\Bigg)\cdot\frac{M_{\mathrm{tot}}}{\sigma_{0,\mathrm{ion,SP1}}}\end{aligned} \tag{7}$$

The intrinsic ionic conductivity of SP1 $\sigma_{0,\mathrm{ion,SP1}}$ can then be dropped, resulting in the following prediction for the relative ionic composite conductivity $\sigma^{\mathrm{Xu}}_{\mathrm{rel,ion,comp}}$:

$$\begin{aligned}\sigma^{\mathrm{Xu}}_{\mathrm{rel,ion,comp}} = &\frac{1}{4}\Bigg(3\,\phi_{\mathrm{SP2,rel}}\,(\lambda_{\mathrm{ion}}-1)+(2-\lambda_{\mathrm{ion}}) \\ &+\sqrt{\left[3\,\phi_{\mathrm{SP2,rel}}\,(\lambda_{\mathrm{ion}}-1)+(2-\lambda_{\mathrm{ion}})\right]^2+8\,\lambda_{\mathrm{ion}}}\Bigg)\cdot M_{\mathrm{tot}}\end{aligned} \tag{8}$$

C.3 Derivation and validation of the relative interface resistivity used in the MST model

In this section, the relative interface resistivity used for the MST-model (Eq. 20 in section 2.3.3 of the main article) is derived. In general, a resistance R is related to a conductivity σ in the following way:

$$\sigma = \frac{L}{A}\frac{1}{R} \tag{9}$$

where L is the length and A the cross section of the conductor. The resistivity ρ is the inverse conductivity:

$$\rho = \frac{1}{\sigma} = \frac{A}{L}R \tag{10}$$

We aim to formulate an interface resistivity $\rho_{\mathrm{I,SP1-SP2}}$ accounting for the interface resistances between SP1 and SP2 as visualized in Fig. 5:

$$\rho_{\mathrm{I,SP1-SP2,ion}} = \frac{A}{2r_{\mathrm{max,SPtot}}}R_{\mathrm{int}} \tag{11}$$

Thereby, R_{int} is the interface resistance and the length L of the conductor is the distance between two interface resistances, which is approximated by the bulge diameter $2r_{\mathrm{max,SPtot}}$. Note that this interface resistivity only accounts for the interface resistances between SP1 and SP2 and not for the transport resistances within SP1 and SP2. It is formulated for the ionic charge transport and will be generalized to include the electronic charge transport later. The interface resistance R_{int} is given by:

$$R_{\mathrm{int}} = \frac{\rho_{\mathrm{int}}}{IA_{\mathrm{V,SP1-SP2}}\cdot A\cdot 2r_{\mathrm{max,SPtot}}} \tag{12}$$

where ρ_{int} is the area specific interface resistance between SP1 and SP2 and $IA_{\mathrm{V,SP1-SP2}}\cdot A\cdot 2r_{\mathrm{max,SPtot}}$ is a measure for the interface area for a characteristic length of the bulges. By inserting Eq. 12 in Eq. 11 we obtain:

$$\rho_{\mathrm{I,SP1-SP2,ion}} = \frac{A}{2r_{\mathrm{max,SPtot}}}\frac{\rho_{\mathrm{int}}}{IA_{\mathrm{V,SP1-SP2}}\cdot A\cdot 2r_{\mathrm{max,SPtot}}} = \frac{\rho_{\mathrm{int}}}{IA_{\mathrm{V,SP1-SP2}}\cdot\left(2r_{\mathrm{max,SPtot}}\right)^2} \tag{13}$$

As we are looking for relative properties, we get rid of the dimension by relating the area specific interface resistance ρ_{int} to the intrinsic conductivity of SP1 $\sigma_{0,\mathrm{ion,SP1}}$.

$$\rho_{\mathrm{rel,I,SP1-SP2,ion}} = \rho_{\mathrm{I,SP1-SP2}}\cdot\sigma_{0,\mathrm{ion,SP1}} = \frac{\rho_{\mathrm{int}}\cdot\sigma_{0,\mathrm{ion,SP1}}}{IA_{\mathrm{V,SP1-SP2}}\cdot\left(2r_{\mathrm{max,SPtot}}\right)^2} \tag{14}$$

where $\nu_{\mathrm{ion}} = \rho_{\mathrm{int}}\cdot\sigma_{0,\mathrm{ion,SP1}}$ can be summarized to a ratio with the unit of a length, relating the area specific interface resistance to the intrinsic conductivity. Therewith, the final expression for the relative interface resistivity reads:

$$\rho_{\mathrm{rel,I,SP1-SP2},i} = \frac{\nu_i}{IA_{\mathrm{V,SP1-SP2}}\cdot\left(2r_{\mathrm{max,SPtot}}\right)^2} \tag{15}$$

where i denotes eon or ion.

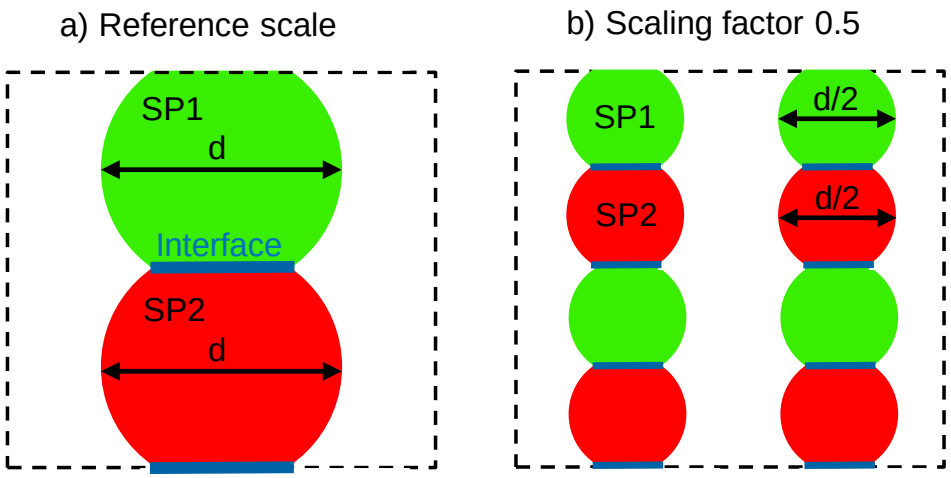

Fig. 5 Illustration of the scaling of the interface resistance.

The analytical expression of the relative interface resistivity (Eq. 15) used in the MST model is validated with the simulation data with porosity $\varepsilon = 50\,\%$,
$\phi_{\mathrm{SP1}} : \phi_{\mathrm{SP2}} = 30 : 70$ and different wetting behaviours (case 1, case 2 and case 4) as a function of ν_{ion} (i.e., normalized area specific interface resistance) as reported in Fig. 4. A very good qualitative and also a good quantitative agreement can be observed compared to the simulation data. This especially confirms the validity of the conclusions formulated in appendix A for the effects related to an interface resistance between the two solid phases.

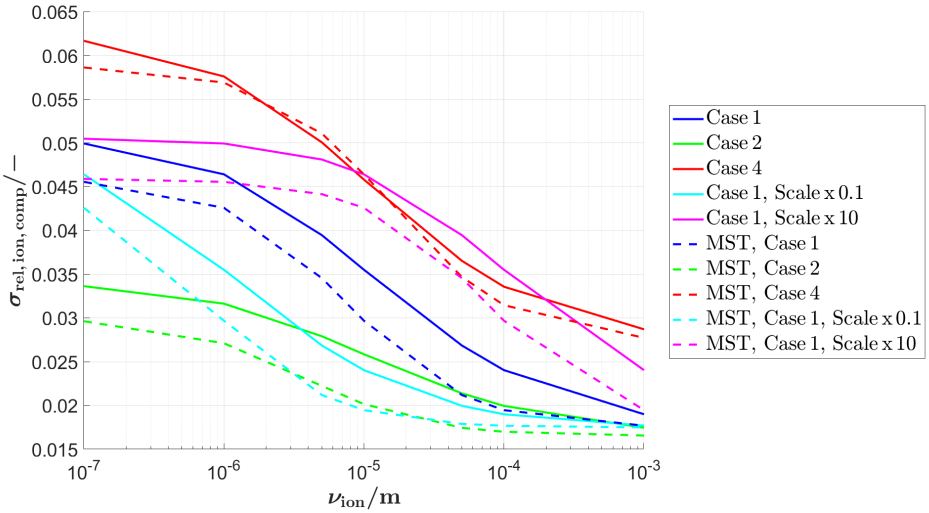

Fig. 6 Relative ionic composite conductivity including interface resistances between SP1 and SP2 for different wetting behaviours (Case 1, Case 2 and Case 4) and comparison with predictions of the MST-model including interface resistances for different scaling and wetting behaviour.

D Model validation for the prediction of the composite conductivity

In this chapter, the validation tests for the semi-analytical models to predict the composite conductivity are reported. The validation for the virtual LSTN-CGO microstructure variation introduced in a previous publication (Marmet et al.[1]) is reported for the Maxwell model (section D.1), the Xu model (section D.2) and the MST model (section D.3). Moreover, validation tests for two further datasets of pure PGM structures and to sphere-packing structures are reported in section D.4, in order to check the sensitivity of the prediction models on the structure type. A summary of the validation is provided in section 3.3 of the main article. An overview of the MAPEs for the different models and conductivity ratios λ is provided in table 2.

Table 2 MAPEs for the different models and different conductivity ratios λ for a dataset of virtual but realistic PGM structures representing LSTN-CGO electrodes with different compositions and porosities.

Conductivity ratio λ	Maxwell model	Xu model	MST model
$\lambda_{\text{ion}} = 0.1$	3.65 %	6.03 %	5.44 %
$\lambda_{\text{eon}} = 0.1$	4.13 %	6.56 %	5.69 %
$\lambda_{\text{ion}} = 0.5$	0.84 %	0.88 %	2.38 %
$\lambda_{\text{ion}} = 0.01$	25.53 %	19.02 %	8.76 %
$\lambda_{\text{eon}} = 0.0001$	692.11 %	65.82 %	53.8 %

D.1 Predictions with the Maxwell model

D.1.1 Validation for conductivity ratio $\lambda = 0.1$

In Fig. 7, the predictions of the relative ionic and electronic composite conductivities for a $\lambda_{\text{ion}} = \lambda_{\text{eon}} = 0.1$ are compared with the corresponding simulation results. As expected, the largest deviations are found for the regions with similar volume fractions of the two solid phases, where the model-assumption of isolated spheres are considerably violated. Nevertheless, a quite good match can be observed between the predictions and the simulations with a $\text{MAPE}_{\text{comp,ion,Max}} = 3.65\,\%$ for the relative ionic and a $\text{MAPE}_{\text{comp,eon,Max}} = 4.13\,\%$ for the relative electronic composite conductivity. A reasonable agreement can be observed for the whole studied range of values of the composite conductivities as reported in the scatter-plots in Fig. 7 b) and d).

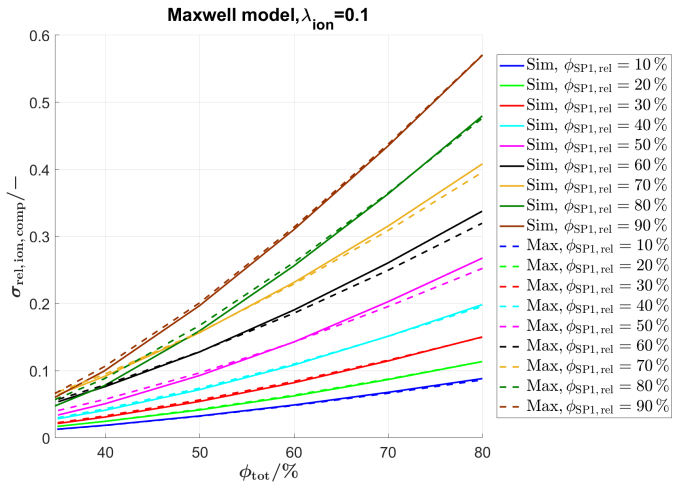

(a) Relative ionic composite conductivity.

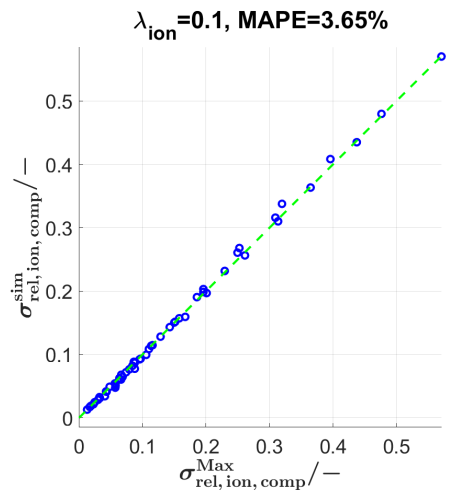

(b) Relative ionic composite conductivity, scatter plot.

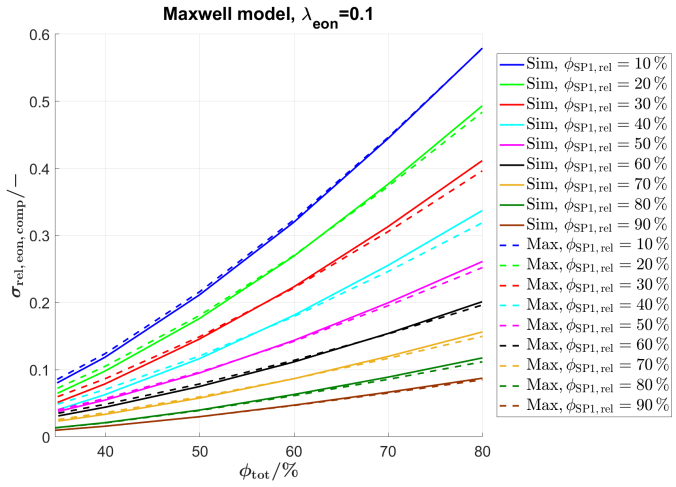

(c) Relative electronic composite conductivity.

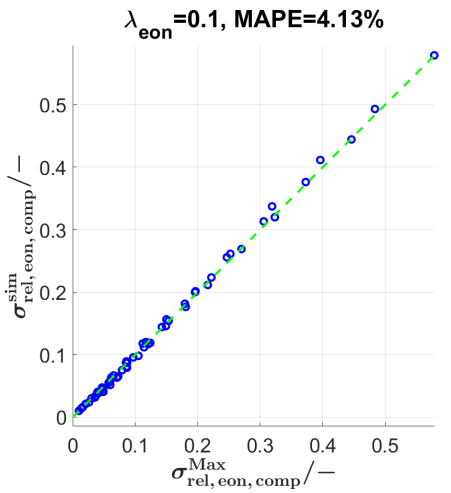

(d) Relative electronic composite conductivity, scatter plot.

Fig. 7 Prediction of the relative composite conductivity with the Maxwell model for a $\lambda_{\text{ion}} = \lambda_{\text{eon}} = 0.1$: comparison of the relative ionic a),b) and relative electronic c),d) composite conductivity for different total solid volume fractions ϕ_{tot} and compositions $\phi_{\text{SP1,rel}}$.

D.1.2 Validation for conductivity ratio $\lambda = [0.5, 0.01, 0.0001]$

The predictions with the Maxwell model are also tested for further conductivity ratios $\lambda = [0.5, 0.01, 0.0001]$, as briefly discussed in section 3.3 of the main article. The corresponding results are summarized in table 2. The comparison with the simulation data and the scatter plots are reported in Fig. 8 for a $\lambda_{\text{ion}} = 0.5$, in Fig. 9 for a $\lambda_{\text{ion}} = 0.01$ and in Fig. 10 for a $\lambda_{\text{eon}} = 0.0001$. For a $\lambda_{\text{ion}} = 0.5$ the $\text{MAPE}_{\text{comp,eon,Max}} = 0.84\,\%$ is considerably smaller compared to $\lambda_{\text{ion}} = 0.1$, probably because the M-factor of the total solid phase is a good

approximation as the intrinsic conductivities of the two solid phases are quite close. For a $\lambda_{\text{ion}} = 0.01$ the prediction is considerably worse compared to $\lambda_{\text{ion}} = 0.1$, especially for lower relative conductivities. However, the prediction with a MAPE $= 28.53\,\%$ is still reasonable and the data is roughly represented. For a $\lambda_{\text{eon}} = 0.0001$, which corresponds to the electronic conductivity ratio of the solid phases for an Ni-CGO electrode, the prediction is relatively good for $\sigma_{\text{rel,eon,comp}} > 0.02$. For $\sigma_{\text{rel,eon,comp}} < 0.02$, which e.g., corresponds to electrodes with high porosities, the data is no more well represented by the prediction. The results from numerical simulations (which are considered to represent the true values) are significantly overestimated by the predictions with the Maxwell model. The overall MAPE $= 692\,\%$ is very large.

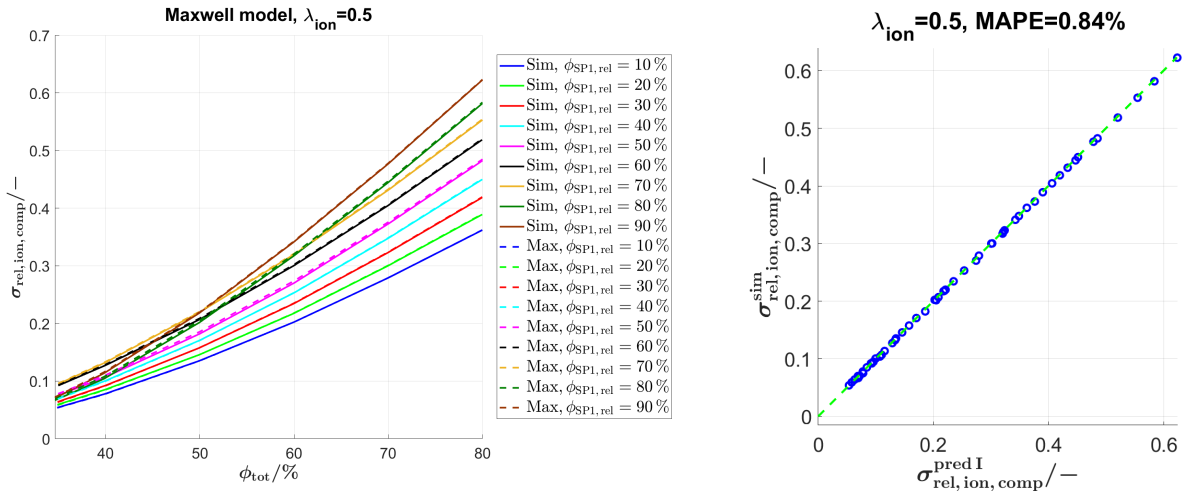

(a) Relative ionic composite conductivity.

(b) Relative ionic composite conductivity, scatter plot.

Fig. 8 Prediction of the relative ionic composite conductivity with the Maxwell model for $\lambda_{\text{ion}} = 0.5$ and comparison with simulation data for different total solid volume fractions ϕ_{tot} and compositions $\phi_{\text{SP1,rel}}$.

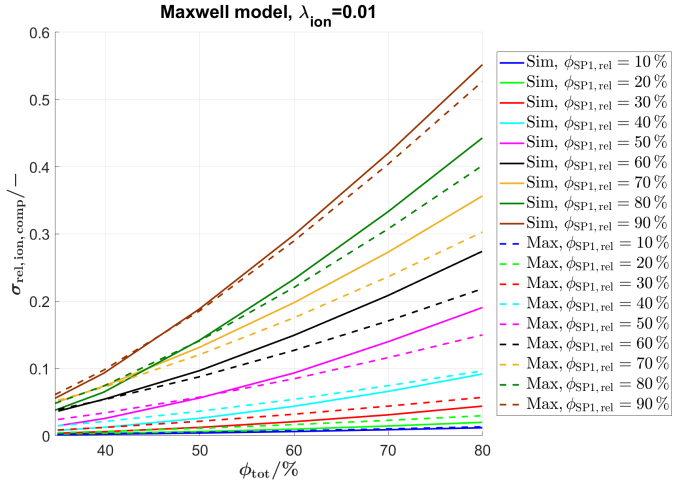

(a) Relative ionic composite conductivity.

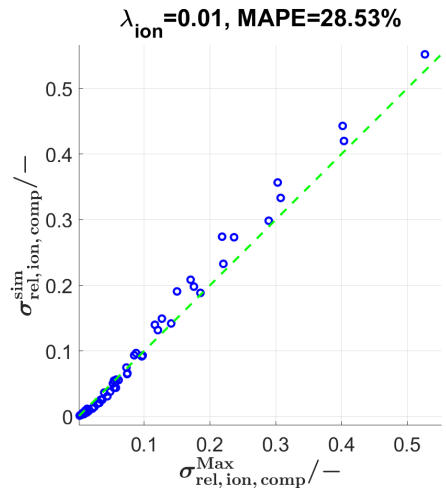

(b) Relative ionic composite conductivity, scatter plot.

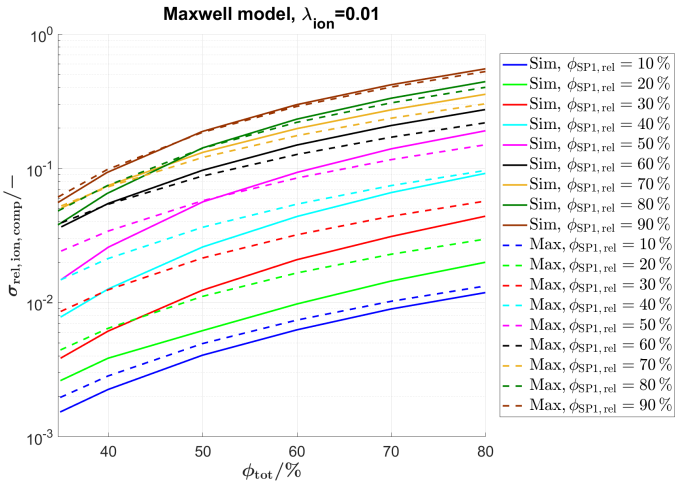

(c) Relative ionic composite conductivity, log-scale.

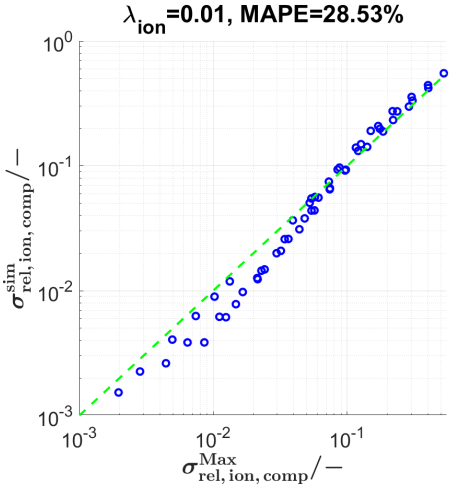

(d) Relative ionic composite conductivity, scatter plot, log-scale.

Fig. 9 Prediction of the relative ionic composite conductivity with the Maxwell model for $\lambda_{ion} = 0.01$ and comparison with simulation data for different total solid volume fractions ϕ_{tot} and compositions $\phi_{SP1,rel}$ using a),b) a linear scale and c),d) a logarithmic scale.

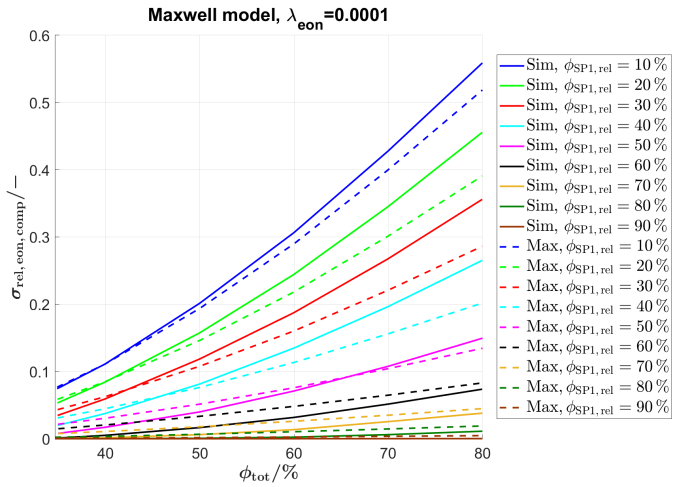

(a) Relative ionic composite conductivity.

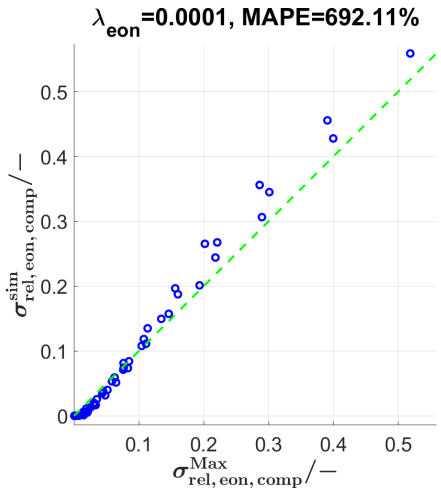

(b) Relative ionic composite conductivity predicted vs simulated

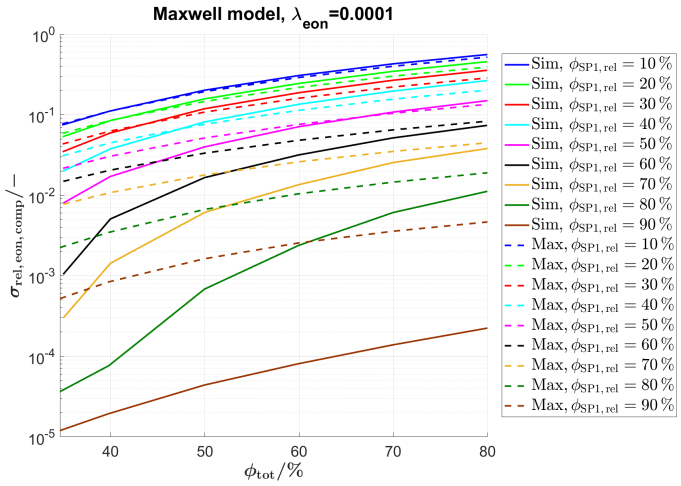

(c) Relative ionic composite conductivity.

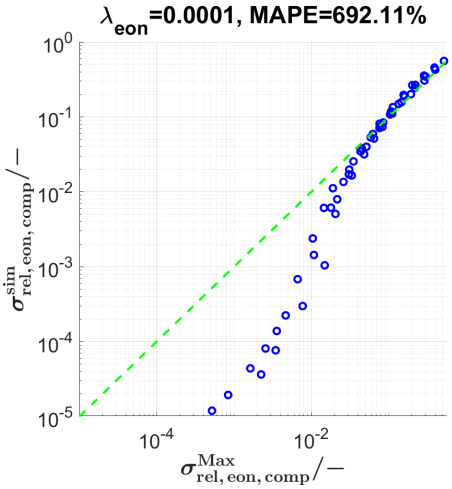

(d) Relative ionic composite conductivity predicted vs simulated

Fig. 10 Prediction of the relative electronic composite conductivity with the Maxwell model for $\lambda_{eon} = 0.0001$ and comparison with simulation data for different total solid volume fractions ϕ_{tot} and compositions $\phi_{SP1,rel}$ using a),b) a linear scale and c),d) a logarithmic scale.

D.2 Predictions with the Xu model

D.2.1 Validation for conductivity ratio $\lambda = 0.1$

The results of the prediction of the relative ionic composite conductivity with the Xu model for a $\lambda_{\text{ion}} = 0.1$ are reported in Fig. 11 together with the corresponding simulation results. A quite good match can be observed between the predictions and the simulations with a $\text{MAPE}_{\text{comp, ion, Xu}} = 6.03\,\%$ for the relative ionic composite conductivity. The prediction quality for high solid volume fractions and similar volume fractions for the two solid phases is better than for the adapted Maxwell model (see section D.1). This is consistent with the modelling assumptions of percolating phases of the Xu model. For low total solid volume fractions and for compositions with very different phase volume fractions for SP1 und SP2, the prediction of the Xu model is worse compared to the Maxwell model, because the assumption of two percolating solid phases does not hold in these regions. The prediction quality for the relative electronic composite conductivity is very similar with a $\text{MAPE}_{\text{comp, eon, Xu}} = 6.56\,\%$ and is reported in Fig. 12. The MAPEs for the relative ionic and electronic composite conductivities for $\lambda_{\text{ion}} = \lambda_{\text{eon}} = 0.1$ are slightly worse compared to the Maxwell model as summarized in table 2.

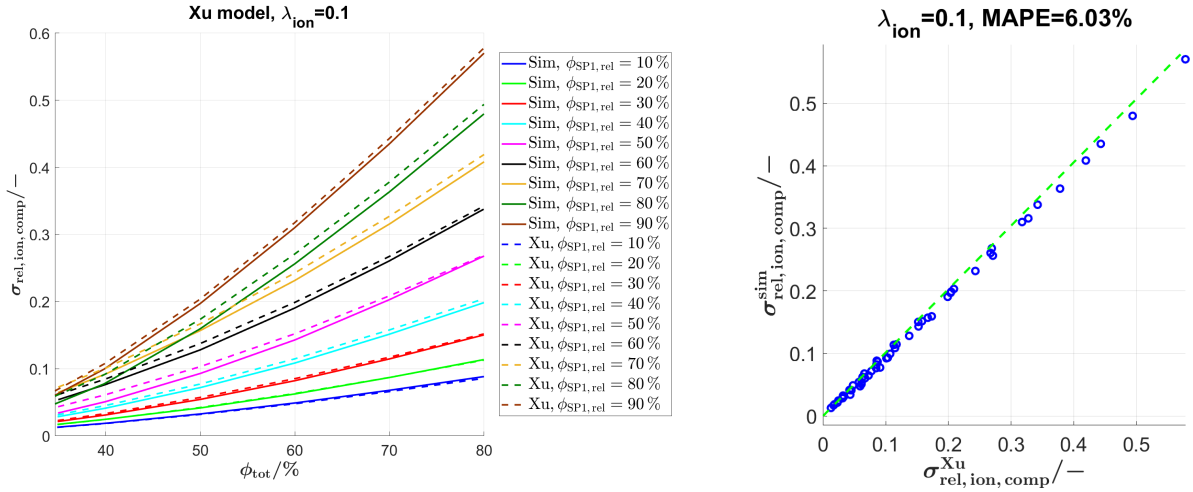

(a) Relative ionic composite conductivity.

(b) Relative ionic composite conductivity, scatter plot.

Fig. 11 Prediction of the relative ionic composite conductivity with the Xu model for $\lambda_{\text{ion}} = 0.1$ and comparison with simulation data for different total solid volume fractions ϕ_{tot} and compositions $\phi_{\text{SP1,rel}}$.

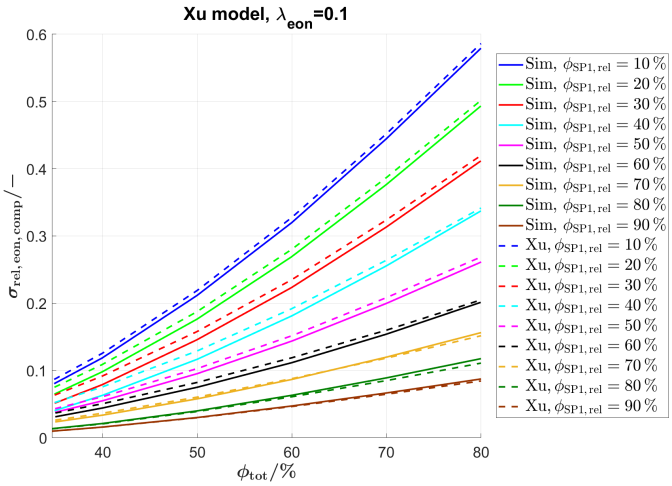

(a) Relative electronic composite conductivity.

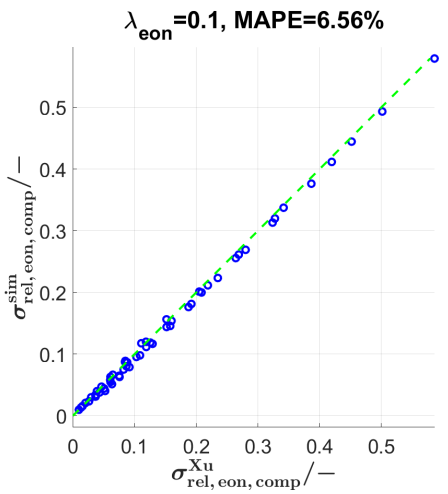

(b) Relative electronic composite conductivity, scatter plot.

Fig. 12 Prediction of the relative electronic composite conductivity with the Xu model for $\lambda_{eon}=0.1$ and comparison with simulation data for different total solid volume fractions ϕ_{tot} and compositions $\phi_{SP1,rel}$.

D.2.2 Validation for conductivity ratio $\lambda=[0.5,0.01,0.0001]$

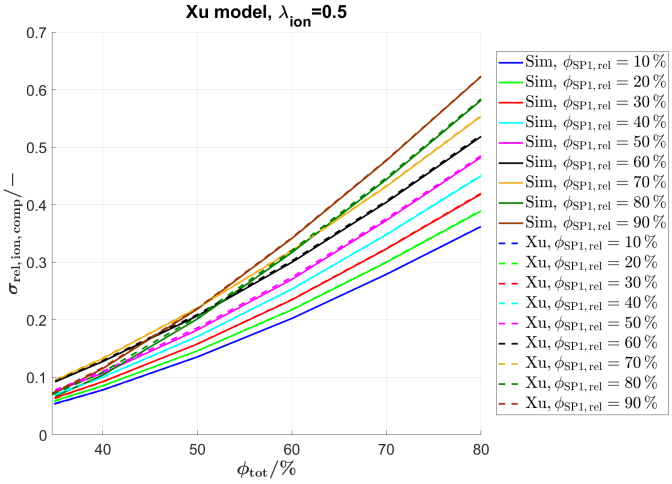

(a) Relative ionic composite conductivity.

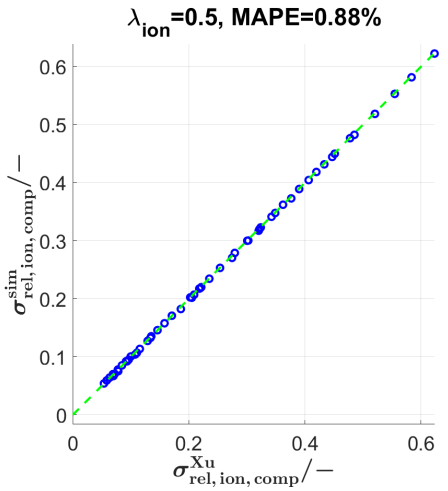

(b) Relative ionic composite conductivity, scatter plot

Fig. 13 Prediction of the relative ionic composite conductivity with the Xu model for $\lambda_{ion}=0.5$ and comparison with simulation data for different total solid volume fractions ϕ_{tot} and compositions $\phi_{SP1,rel}$.

The predictions with the Xu model are also tested for further conductivity ratios $\lambda=[0.5,0.01,0.0001]$, as briefly discussed in section 3.3 of the main article. The corresponding results are summarized in table 2. The comparison with the simulation data and the scatter plots are reported in Fig. 12, in Fig. 13 for a $\lambda_{ion}=0.5$, in Fig. 14 for a $\lambda_{ion}=0.01$ and in Fig. 15 for a $\lambda_{eon}=0.0001$. For a $\lambda_{ion}=0.5$ the MAPE $=0.88\,\%$ is considerably smaller compared to $\lambda=0.1$ as already observed for the Maxwell model. For $\lambda_{ion}=0.01$, the prediction is considerably worse compared to $\lambda_{ion}=0.1$, especially for intermediate M-factors in the region of 0.01 to 0.1. However, the prediction with a MAPE $=19.02\,\%$ is still reasonable and the data is roughly represented. Moreover, the MAPE is considerably smaller than for the Maxwell model (19.02% compared to 25.53%). For a $\lambda_{eon}=0.0001$, the prediction is relatively good for relative composite conductivities $\sigma_{rel,eon,comp}>0.02$. For the region $\sigma_{rel,eon,comp}=0.0001-0.02$, which is around the percolation threshold of SP2 (e.g., the Ni-phase), the deviations to the simulation results are very large (more than one order of magnitude). For very low $\sigma_{rel,eon,comp}<0.0001$, the predictions are again quite good. To sum it up, the Xu model is not able to predict

the percolation-threshold of the SP2 (e.g., Ni-phase). However, this was also not expected as this depends on geometrical details of the microstructure, which are not modelled. Apart from this deficiency, the prediction of the composite conductivity with the Xu model shows a good agreement with the results from numerical transport simulation. Moreover, the Xu model is more robust compared to the Maxwell model.

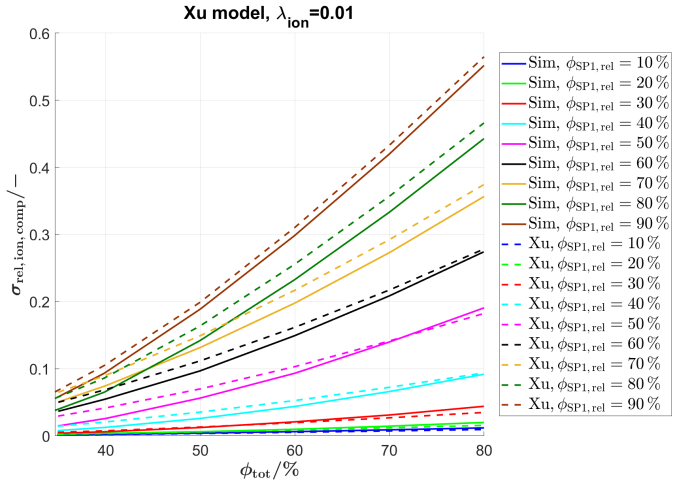

(a) Relative ionic composite conductivity.

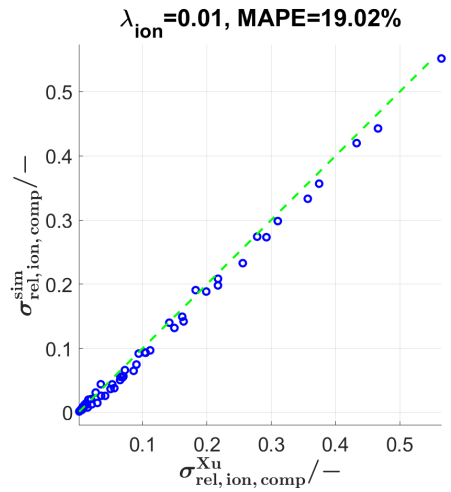

(b) Relative ionic composite conductivity, scatter plot.

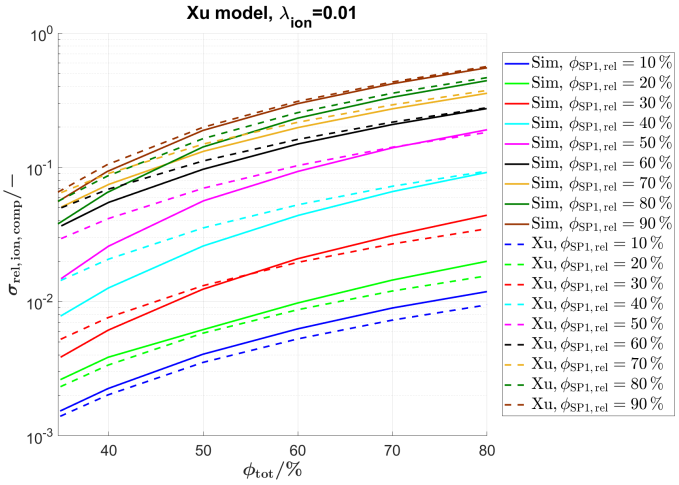

(c) Relative ionic composite conductivity, log-scale.

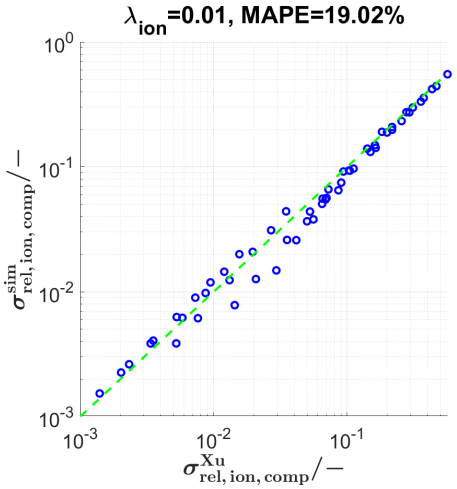

(d) Relative ionic composite conductivity, scatter plot, log-scale.

Fig. 14 Prediction of the relative ionic composite conductivity with the Xu model for $\lambda_{ion} = 0.01$ and comparison with simulation data for different total solid volume fractions ϕ_{tot} and compositions $\phi_{SP1,rel}$ using a),b) a linear scale and c),d) a logarithmic scale.

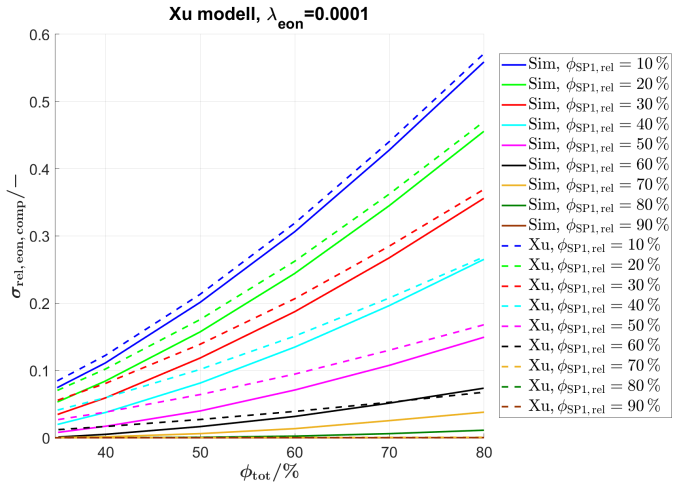

(a) Relative electronic composite conductivity.

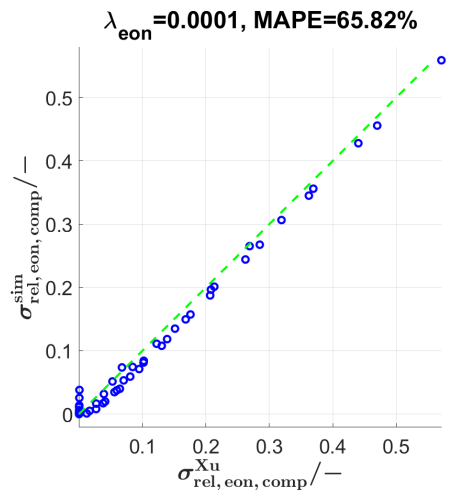

(b) Relative electronic composite conductivity, scatter plot.

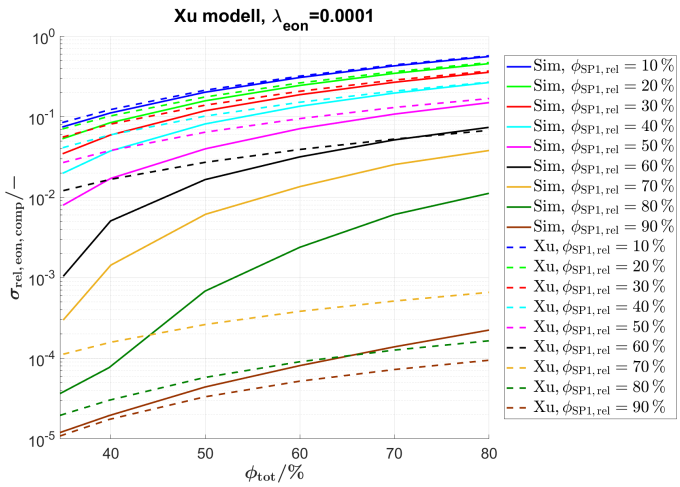

(c) Relative electronic composite conductivity, log-scale.

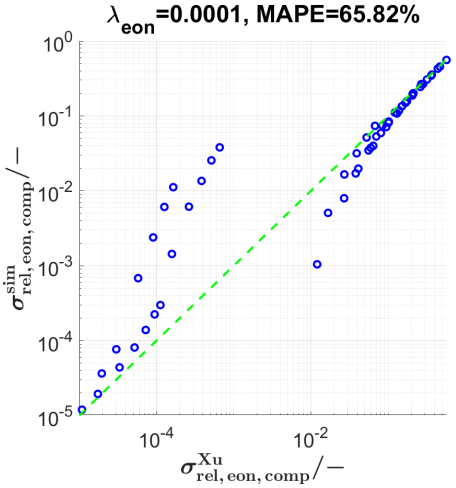

(d) Relative electronic composite conductivity, scatter plot, log-scale.

Fig. 15 Prediction of the relative electronic composite conductivity with the Xu model for $\lambda_{eon} = 0.0001$ and comparison with simulation data for different total solid volume fractions ϕ_{tot} and compositions $\phi_{SP1,rel}$ using a),b) a linear scale and c),d) a logarithmic scale.

D.3 Predictions with the MST model

D.3.1 Validation for conductivity ratio $\lambda = 0.1$

For the MST model, the exponent a in Eq. 18 of the main article needs to be fitted in order to achieve a good prediction quality. A fixed exponent $a = 0.6$ provides good prediction qualities for all the data used in this work and is thus used for all predictions with the MST model. The results of the prediction of the relative ionic composite conductivity with the MST model for a $\lambda_{\text{ion}} = 0.1$ are reported in Fig. 16 together with the simulation results. A quite good match can be observed between the predictions and the simulations with a $\text{MAPE}_{\text{comp, ion, MST}} = 5.44\,\%$ for the relative ionic composite conductivity, which is in the same range as for the Maxwell and the Xu model. The prediction quality of the relative electronic composite conductivity is again very similar with a $\text{MAPE}_{\text{comp, eon, Xu}} = 5.69\,\%$ and is reported in Fig. 17.

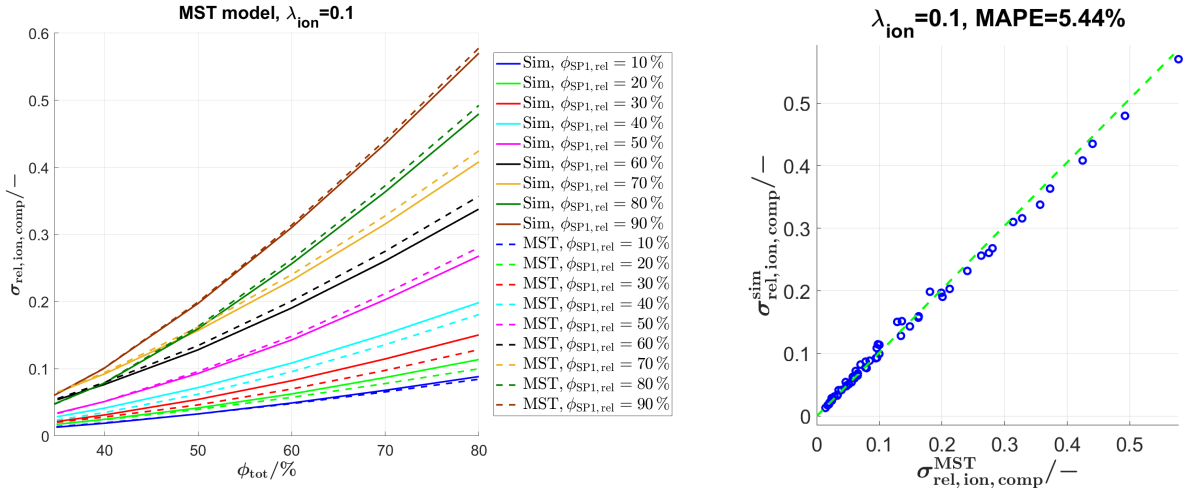

(a) Relative ionic composite conductivity.

(b) Relative ionic composite conductivity, scatter plot.

Fig. 16 Prediction of the relative ionic composite conductivity with the MST model for $\lambda_{\text{ion}} = 0.1$ and comparison with simulation data for different total solid volume fractions ϕ_{tot} and compositions $\phi_{\text{SP1,rel}}$.

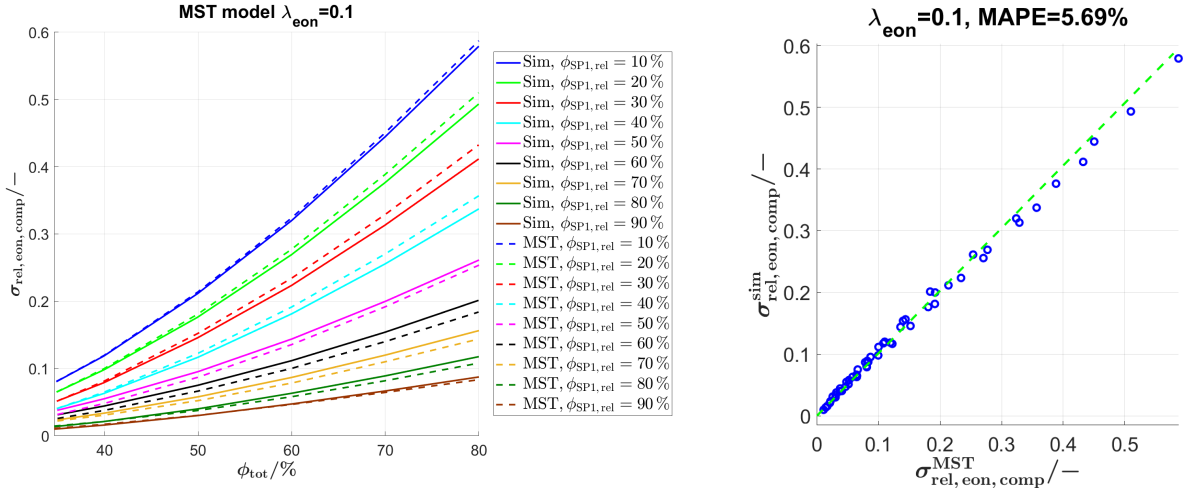

(a) Relative electronic composite conductivity.

(b) Relative electronic composite conductivity, scatter plot.

Fig. 17 Prediction of the relative electronic composite conductivity with the MST model for $\lambda_{\text{eon}} = 0.1$ and comparison with simulation data for different total solid volume fractions ϕ_{tot} and compositions $\phi_{\text{SP1,rel}}$.

D.3.2 Validation for conductivity ratio $\lambda = [0.5, 0.01, 0.0001]$

The predictions with the MST model are also tested for further conductivity ratios $\lambda = 0.5, 0.01, 0.0001$, as briefly discussed in section 3.3 of the main article. The corresponding results are summarized in table 2. The comparison with the simulation data and the scatter plots are reported in Fig. 18 for a $\lambda_{\mathrm{ion}} = 0.5$, in Fig. 19 for a $\lambda_{\mathrm{ion}} = 0.01$ and in Fig. 20 for a $\lambda_{\mathrm{eon}} = 0.0001$.

For a $\lambda_{\mathrm{ion}} = 0.5$ the $\mathrm{MAPE}_{\mathrm{comp,ion,MST}} = 2.38\,\%$ is considerably smaller compared to $\lambda = 0.1$ but also about two times higher compared to the Maxwell and Xu model, where the approximation with the total M-factor fits especially well for the two models. For a $\lambda_{\mathrm{ion}} = 0.01$, the prediction is only slightly worse compared to $\lambda_{\mathrm{ion}} = 0.1$ with a MAPE $= 8.76\,\%$ and the MAPE is more than a factor of two lower compared to the Maxwell and the Xu model. For $\lambda_{\mathrm{eon}} = 0.0001$, the prediction is very good for relative electronic composite conductivities $\sigma_{\mathrm{rel,eon,comp}} > 0.001$, which is a much larger range than for the Maxwell and the Xu model only providing reasonable results for $\sigma_{\mathrm{rel,eon,comp}} > 0.02$. The overall MAPE $= 53.8\,\%$ is still quite high, but considerably smaller than for the Maxwell and the Xu model.

In summary, the MST model shows similar deviations for $\lambda \geq 0.1$ but performs considerably better for $\lambda < 0.1$ compared to the Maxwell and the Xu model, because the geometrical details of the single phases are captured better due to inclusion of the M-factors of the single phases. This comes at the cost of additional computationally expenses for the characterization of the single phases and an additional fit-factor.

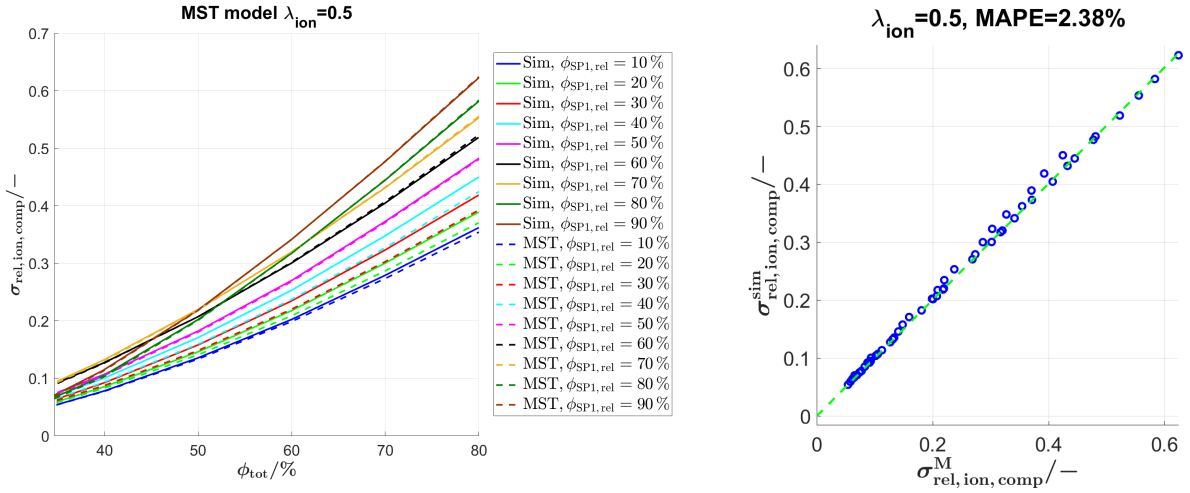

(a) Relative ionic composite conductivity.

(b) Relative ionic composite conductivity, scatter plot.

Fig. 18 Prediction of the relative ionic composite conductivity with the MST model for $\lambda_{\mathrm{ion}} = 0.5$ and comparison with simulation data for different total solid volume fractions ϕ_{tot} and compositions $\phi_{\mathrm{SP1,rel}}$.

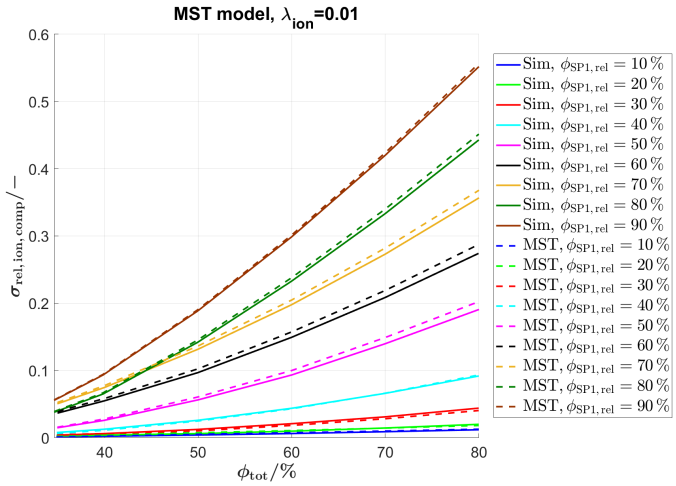

(a) Relative ionic composite conductivity.

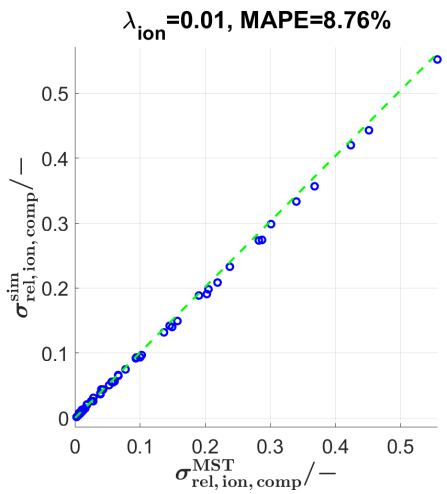

(b) Relative ionic composite conductivity, scatter plot.

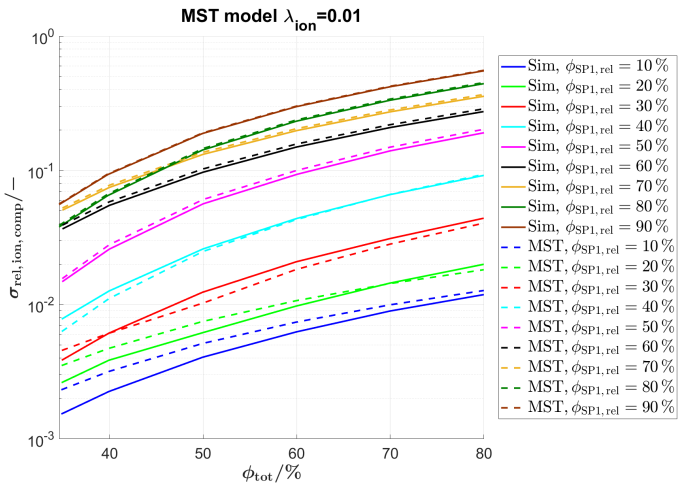

(c) Relative ionic composite conductivity, log-scale.

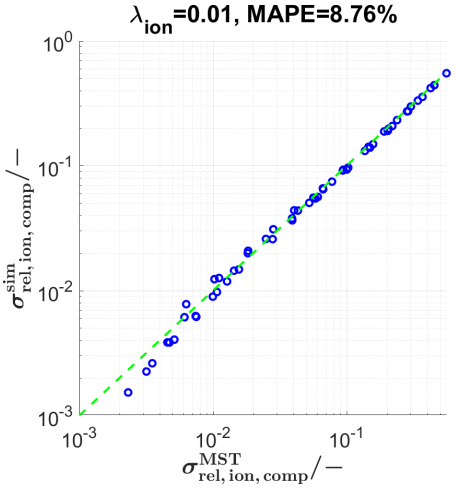

(d) Relative ionic composite conductivity prediction, scatter plot, log-scale.

Fig. 19 Prediction of the relative ionic composite conductivity with the MST model for $\lambda_{ion} = 0.01$ and comparison with simulation data for different total solid volume fractions ϕ_{tot} and compositions $\phi_{SP1,rel}$ using a),b) a linear scale and c),d) a logarithmic scale.

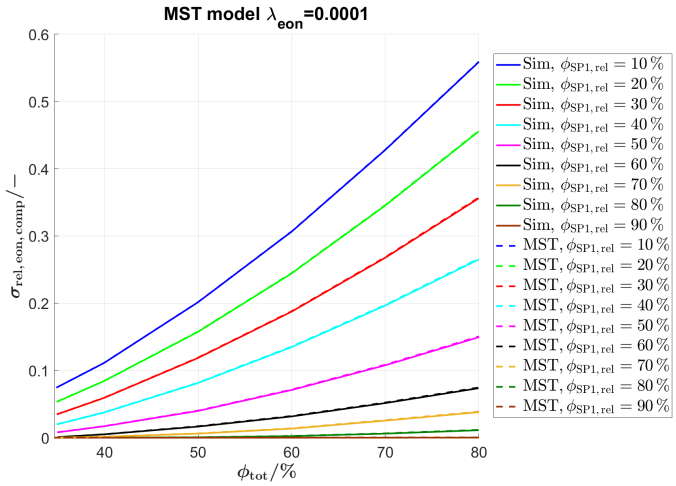

(a) Relative electronic composite conductivity.

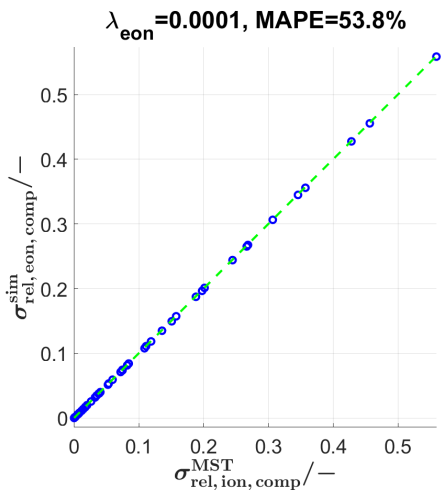

(b) Relative electronic composite conductivity, scatter plot.

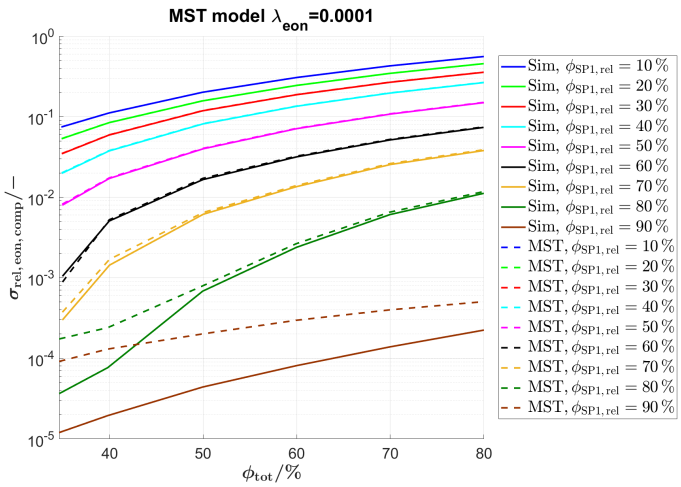

(c) Relative electronic composite, log-scale.

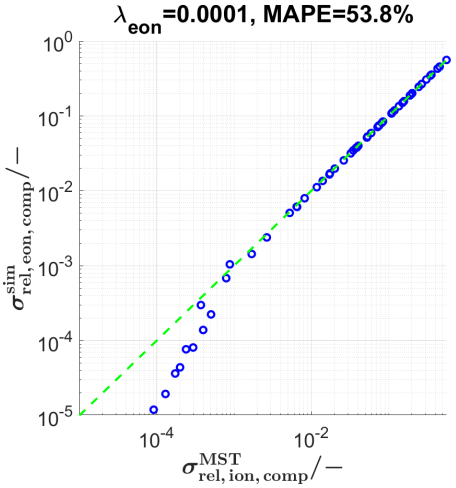

(d) Relative electronic composite conductivity, scatter plot, log-scale.

Fig. 20 Prediction of the relative electronic composite conductivity with the MST model for $\lambda_{eon} = 0.0001$ and comparison with simulation data for different total solid volume fractions ϕ_{tot} and compositions $\phi_{SP1,rel}$ using a),b) a linear scale and c),d) a logarithmic scale.

D.4 Validation of the composite conductivity predictions with further reference data

In order to check the sensitivity of the composite conductivity prediction models on the structure type, they are tested for two further datasets of pure PGM structures and to sphere-packing structures.

D.4.1 Validation of the predictions for a dataset of pure PGM-structures

The dataset of pure PGM structures was reported in a previous publication (Marmet et al.[1]). In contrast to the LSTN-CGO dataset, a neutral wetting behaviour of the phases and no modifications by morphological operations were used. Apart from that, the two structure types are quite similar.

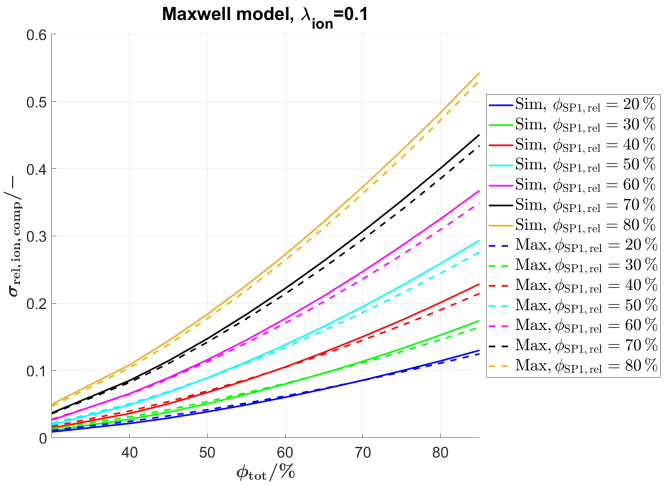

(a) Relative ionic composite conductivity, $\lambda_{ion}=0.1$.

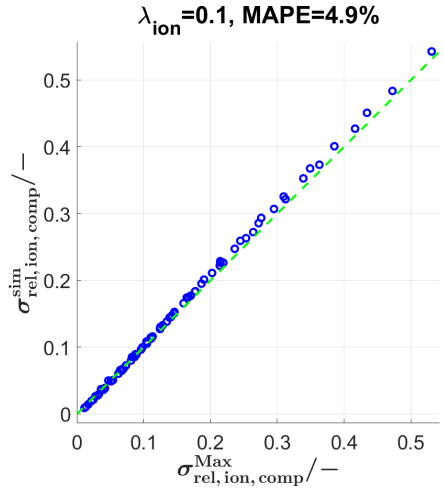

(b) Relative ionic composite conductivity, $\lambda_{ion}=0.1$, scatter plot.

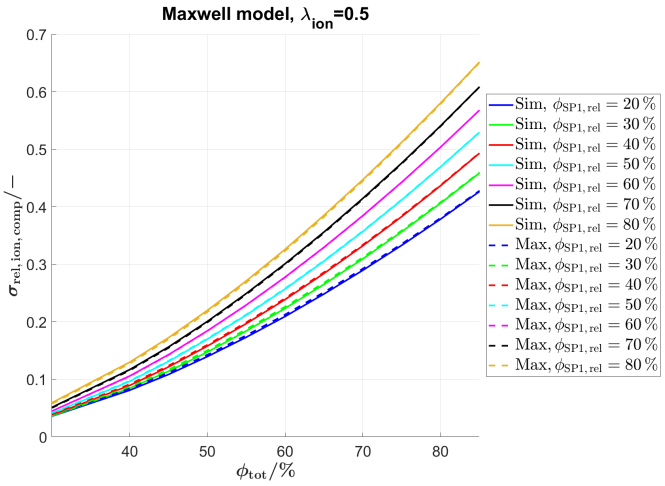

(c) Relative ionic composite conductivity, $\lambda_{ion}=0.1$.

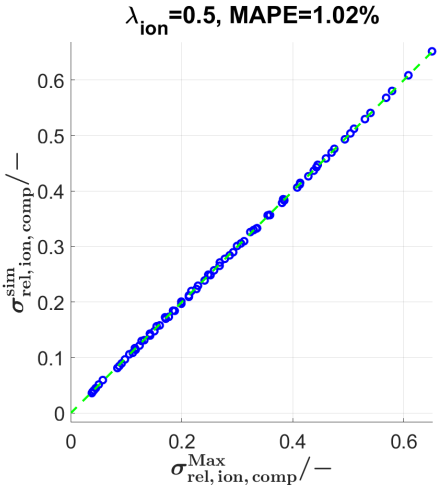

(d) Relative ionic composite conductivity, $\lambda_{ion}=0.5$, scatter plot.

Fig. 21 Validation with a pure PGM dataset: prediction of the relative ionic composite conductivity with the Maxwell model and comparison with simulation data for different total solid volume fractions ϕ_{tot} and compositions $\phi_{SP1,rel}$, for a),b) $\lambda_{ion}=0.1$ and c),d) $\lambda_{ion}=0.5$.

The results of the predictions for the ionic composite conductivities are plotted together with the simulated data for a $\lambda_{ion}=0.1$ and a $\lambda_{ion}=0.5$ in Fig. 21 for the Maxwell model, in Fig. 22 for the Xu model and in Fig. 23 for the MST model. The results are discussed in section D.4. The MAPEs for the relative ionic composite conductivity predictions are summarized in table 3 for the three prediction models and for a $\lambda_{ion}=0.1$ and a $\lambda_{ion}=0.5$. The results are reported in more detail in section D.4.1 in the appendix. The comparison with table 2 shows that the MAPEs of the two datasets (i.e., LSTN-CGO and pure PGM) are very similar. This confirms a minimal robustness of the prediction models for slightly different structure types.

Table 3 MAPEs for the different models and different conductivity ratios λ for a dataset of pure PGM structures with different compositions and porosities reported in a previous publication (Marmet et al.[1]).

Conductivity ratio λ	Maxwell model	Xu model	MST model
$\lambda_{\text{ion}} = 0.1$	4.9 %	4.73 %	3.83 %
$\lambda_{\text{ion}} = 0.5$	1.02 %	1.04 %	2.2 %

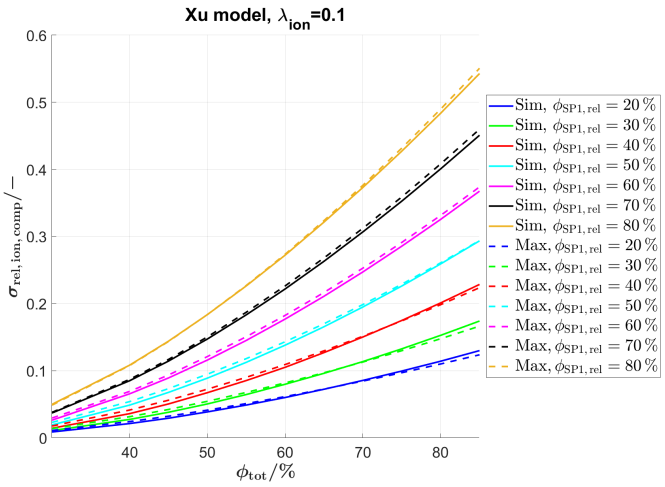

(a) Relative ionic composite conductivity, $\lambda_{\text{ion}} = 0.1$.

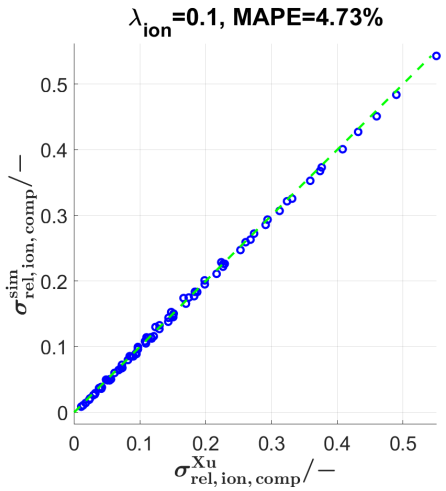

(b) Relative ionic composite conductivity, $\lambda_{\text{ion}} = 0.1$, scatter plot.

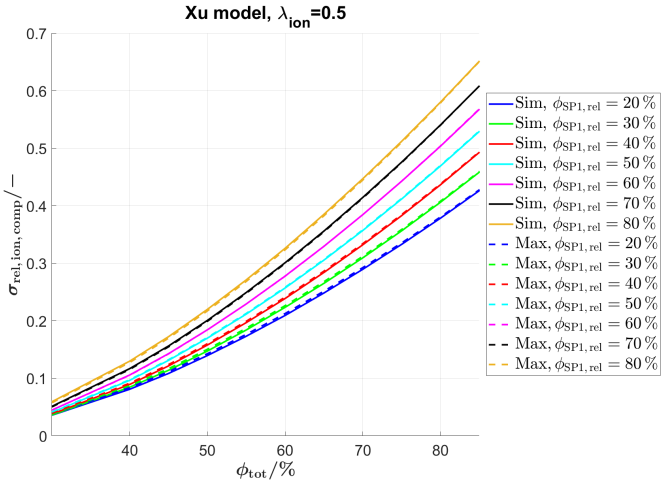

(c) Relative ionic composite conductivity, $\lambda_{\text{ion}} = 0.5$.

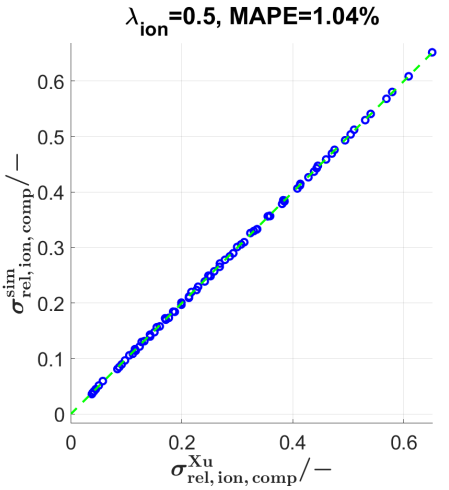

(d) Relative ionic composite conductivity, $\lambda_{\text{ion}} = 0.5$, scatter plot.

Fig. 22 Validation with a pure PGM dataset: prediction of the relative ionic composite conductivity with the Xu model and comparison with simulation data for different total solid volume fractions ϕ_{tot} and compositions $\phi_{\text{SP1,rel}}$, for a),b) $\lambda_{\text{ion}} = 0.1$ and c),d) $\lambda_{\text{ion}} = 0.5$.

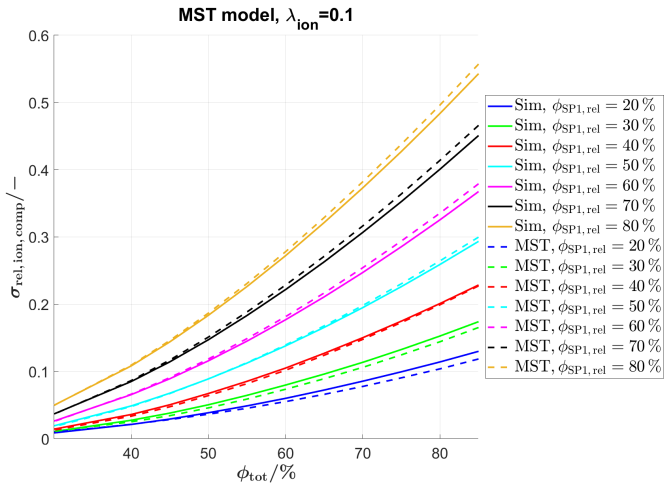

(a) Relative ionic composite conductivity, $\lambda_{ion} = 0.1$.

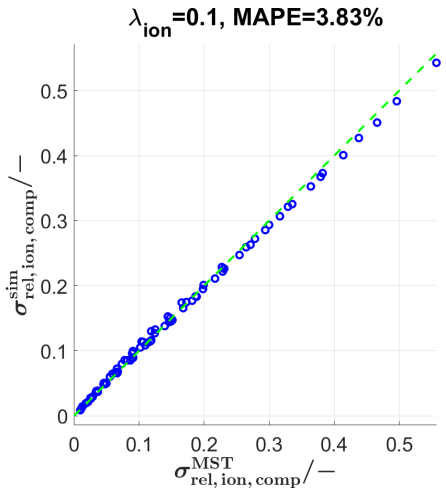

(b) Relative ionic composite conductivity, $\lambda_{ion} = 0.1$, scatter plot.

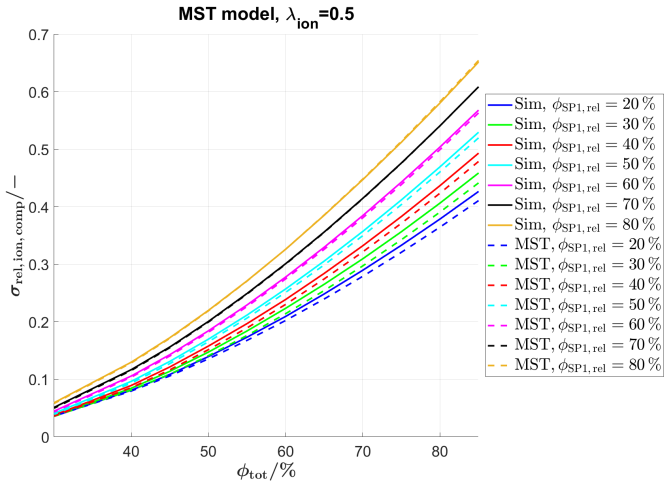

(c) Relative ionic composite conductivity, $\lambda_{ion} = 0.5$.

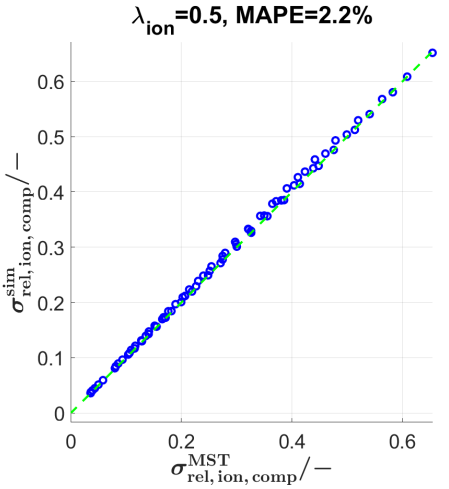

(d) Relative ionic composite conductivity, $\lambda_{ion} = 0.5$, scatter plot.

Fig. 23 Validation with a pure PGM dataset: prediction of the relative ionic composite conductivity with the Xu model and comparison with simulation data for different total solid volume fractions ϕ_{tot} and compositions $\phi_{SP1,rel}$, for a),b) $\lambda_{ion} = 0.1$ and c),d) $\lambda_{ion} = 0.5$.

D.4.2 Validation of the predictions for a dataset of virtual sphere-packing structures

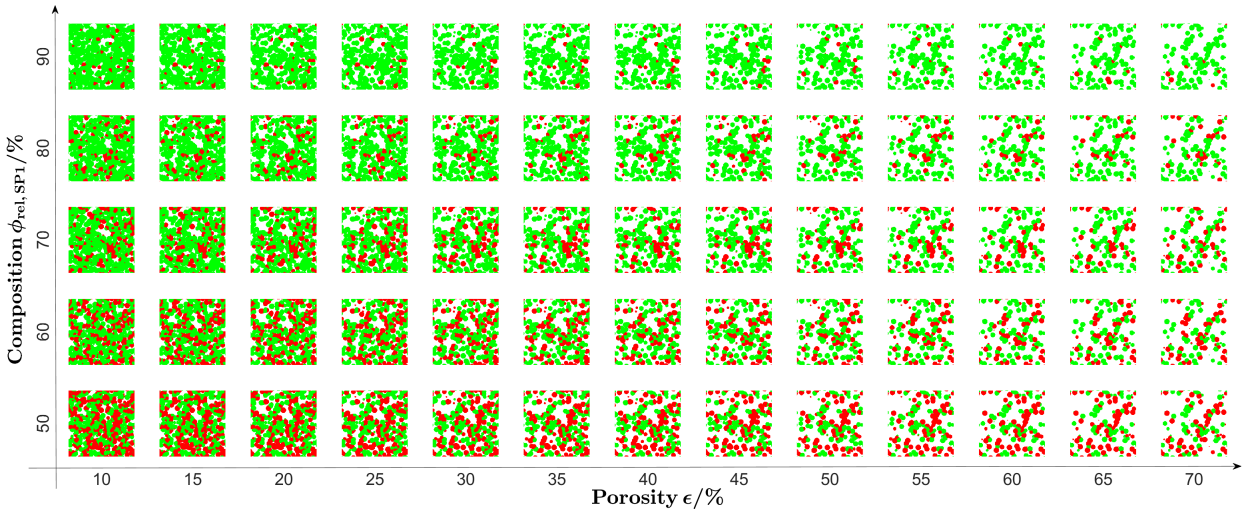

Fig. 24 Set of 65 sphere-packing structures generated using the GrainGeo module of GeoDict. The central orthoslices of the 3D structures are reported for different porosities ε and compositions (i.e., relative volume fraction of SP1 $\phi_{\mathrm{SP1,rel}}$, respectively). Colour code: green = SP1, red = SP2, white = pore.

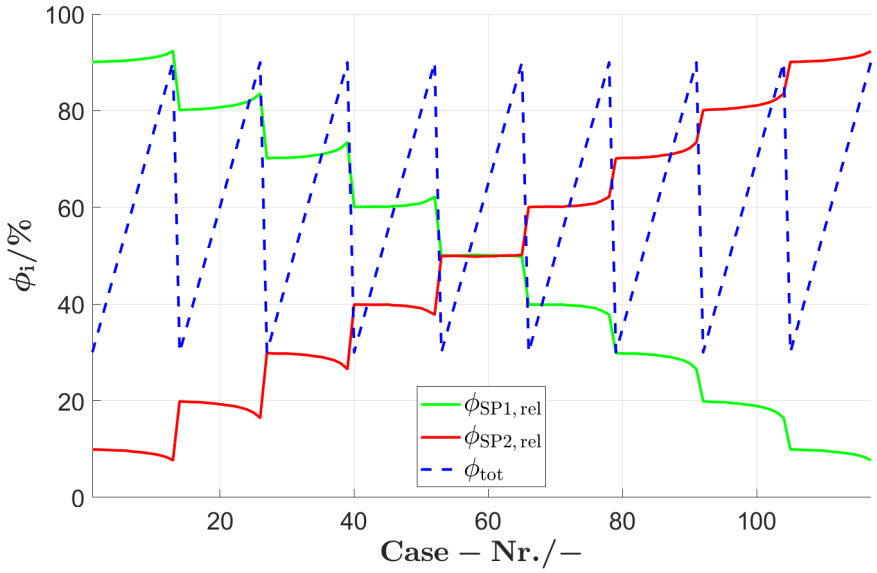

Fig. 25 Relative volume fractions of SP1 $\phi_{\mathrm{SP1,rel}}$ and SP2 $\phi_{\mathrm{SP2,rel}}$ and total solid volume fractions ϕ_{tot} for the set of 117 cases of the sphere-packing structures.

In this section, the three prediction models (Maxwell, Xu and MST) are tested for a dataset of 65 virtual sphere-packing structures reported in Fig. 24, which represent a very different type of microstructure with much more pronounced bottlenecks for the solid phases compared to the LSTN-CGO and to the pure PGM datasets. The 65 sphere-packing structures are constructed with the GrainGeo module of GeoDict[4] using a structure size of 300^3 voxels and a voxel size of 10 nm. Two solid-phases are used, both with a constant sphere diameter of 0.25 µm with uniform distribution in space. The spheres are placed with the "Enforce Overlap" mode and the overlaps of spheres of different materials (SP1 and SP2) are resolved. The remaining space is allocated to the pore-phase. The porosity is varied in the range ε =[10,15,20,25,30,35,40,45,50,55,60,65,70] % (which corresponds to a variation of the total solid vol-

ume fractions in the range of ϕ_{tot} =[90,85,75,60,65,60,55,50,45,40,35,30] %) and the composition of the two solid phases SP1 and SP2 is varied in the range of SP1:SP2 = [50:50,60:40,70:30,80:20,90:10]. As the construction and characterization of these structures is symmetric with respect to SP1 and SP2, SP1 and SP2 are interchanged in order to extend the range of the compositions by SP1:SP2 = [10:90,20:80,30:70,40:60], resulting in a total number of 117 cases. The relative volume fractions of SP1 $\phi_{SP1,rel}$ and SP2 $\phi_{SP2,rel}$ and the total solid volume fraction ϕ_{tot} for the set of 117 cases are reported in Fig. 25. The total solid volume fractions ϕ_{tot} (and therewith the porosities) are matched quite well by the GrainGeo algorithm. In contrast, there is considerable deviation of the realized compositions (i.e., $\phi_{SP1,rel}$ and $\phi_{SP2,rel}$) compared to the defined compositions, as can be observed in Fig. 25. However, these deviations from the defined compositions do not affect the accuracy of the study, as the realized compositions can also be used as input parameters for the prediction models.

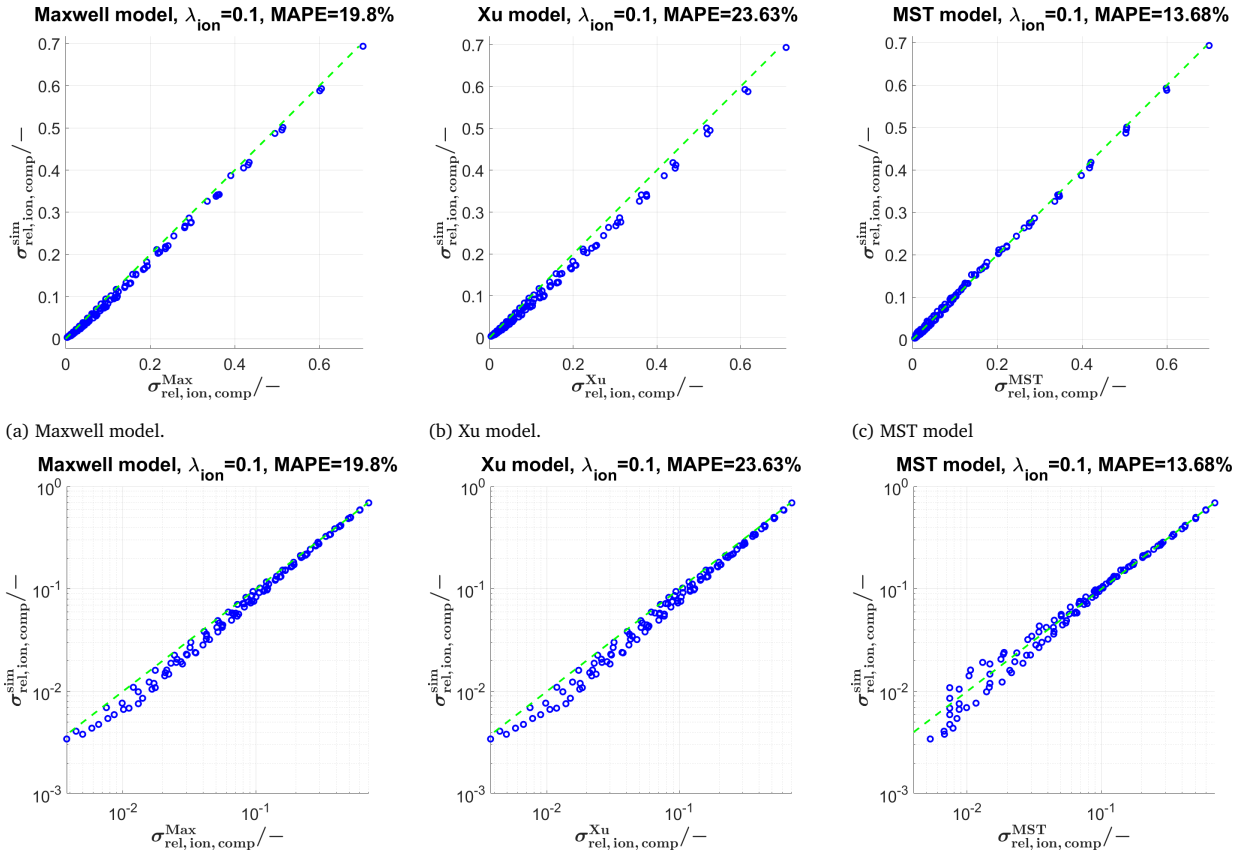

(a) Maxwell model. (b) Xu model. (c) MST model

(d) Maxwell model, log-scale. (e) Xu model, log-scale. (f) MST model, log-scale

Fig. 26 Simulation results vs prediction of the ionic composite conductivity for a dataset of virtual sphere-packing structures with $\lambda_{ion} = 0.1$ for a), d) Maxwell model, b),e) Xu model and c),f) MST model in linear and logarithmic scale.

In Fig. 26 the simulated results are plotted versus the three predictions of the ionic composite conductivity with a $\lambda_{ion} = 0.1$. The MAPEs for the relative ionic composite conductivity predictions are summarized in table 4. The MAPEs for the predictions for the sphere-packing dataset are generally by a factor of about 4 higher than the predictions for the PGM structures (i.e., LSTN-CGO and to the pure PGM datasets, MAPEs reported in tables 2 and 3). This is most probably a result of the pronounced bottlenecks of the sphere-packing structures. Consistently, the MAPE for the MST model including information of the single solid-phases is considerably lower than for the other two predictions, which only take into account the morphology of the total solid-phase. However, for the Maxwell and the Xu model, the predictions systematically overestimate the relative ionic composite conductivity as reported in section 4 in the appendix. Thus, these predictions can be improved with a correction factor accounting for the specific structure type of the sphere-packing. The scatter plots for the Maxwell and the Xu model with a correction factor of 0.9 are reported in Fig. 27. The

corresponding MAPEs are thereby reduced by about 40 %, as reported in table 4. However, there is a clear drawback concerning the loss of generality using such correction factors. For the MST model (Fig. 25 c) and f)) there is no systematic deviation and thus, there is no obvious way to reduce the MAPE using correction factors.

Table 4 MAPEs for the different models and different conductivity ratios λ for a dataset of sphere-packing structures with different compositions and porosities reported in section in the appendix.

Conductivity ratio λ	Maxwell model	Xu model	MST model
$\lambda_{\mathrm{ion}} = 0.1$	19.8 %	23.63 %	13.66 %
$\lambda_{\mathrm{ion}} = 0.1$, correction factor of 0.9	11.91 %	14.05 %	-

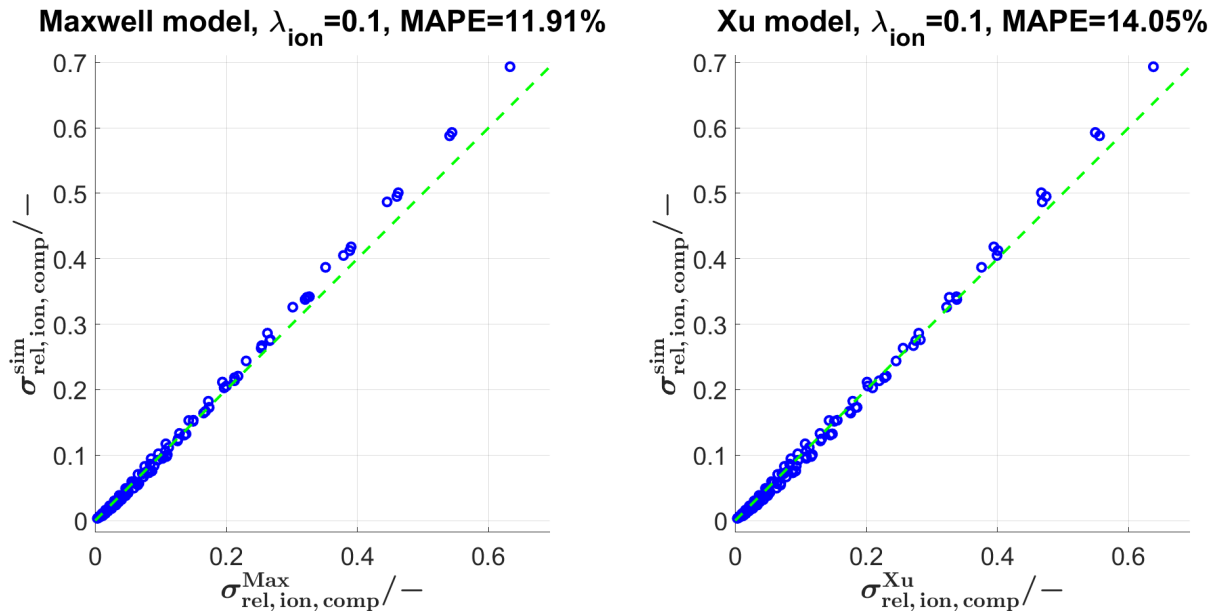

(a) Maxwell model.

(b) Xu model.

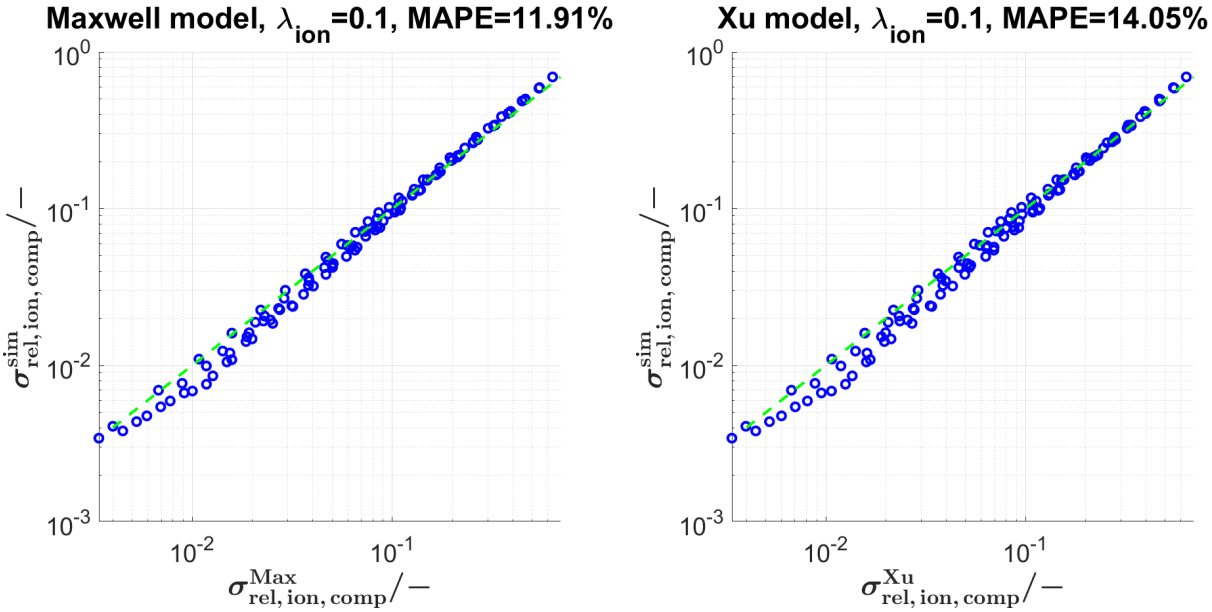

(c) Maxwell model, log-scale.

(d) Xu model, log-scale.

Fig. 27 Correction factor: Simulation results vs prediction of the ionic composite conductivity for a dataset of virtual sphere-packing structures with $\lambda_{\mathrm{ion}} = 0.1$ for a), c) Maxwell model, b),d) Xu model with a correction factor of 0.9.

As a summary, the prediction power of the three prediction models is not independent from the structure type. The most reliable results can be obtained with the MST model, which is, however, also to most expensive one concerning the needed input parameters. Nevertheless, all three models show a reasonable agreement with the simulation data and the deviations are in a good range with respect to other uncertainties like from intrinsic conductivities, contact and interface resistances. Moreover, especially the predictions based on the Maxwell and the Xu model provide a fast and inexpensive possibility to estimate the conductivities of MIEC-based composite electrodes, only requiring the composition, the porosity the intrinsic conductivities and the M-factor of the total solid-phase as input parameters. Composition and porosity can be determined based on 2D images of the electrode appropriately. The M-factor of the total solid-phase generally requires a 3D-image for an accurate representation. However, it can be reasonably estimated using reference datasets as for example reported in this thesis. Thus, the prediction models are especially helpful for a fast screening of suitable material systems and might be selectively complemented with more sophisticated stochastic modelling approaches as reported in a previous publication (Marmet et al.[1]).

References

1 P. Marmet, L. Holzer, T. Hocker, V. Muser, G. K. Boiger, M. Fingerle, S. Reeb, D. Michel and J. M. Brader, *Energy Advances*, 2023, **2**, 1942–1967.

2 P. Marmet, L. Holzer, T. Hocker, G. K. Boiger, H. Bausinger, A. Mai, M. Fingerle, S. Reeb, D. Michel and J. M. Brader, *Energy Advances*, 2023, **2**, 980 – 1013.

3 J. Z. Xu, B. Z. Gao and F. Y. Kang, *Applied Thermal Engineering*, 2016, **102**, 972–979.

4 *GeoDict simulation software Release 2023 (Revision 61624), by Math2Market GmbH, Germany, DOI: 10.30423/release.geodict2023*.